Early embryogenesis in CHDFIDD mouse model reveals facial clefts and altered cranial neurogenesis

Marek Hampl[1,2], Nela Jandova[1,2], Denisa Luskova[1], Monika Novakova[3], Tereza Szotkowska[1], Stepan Cada[2], Jan Prochazka[4,5], Jiri Kohoutek[2], Marcela Buchtova[1,2,*]

[1]Laboratory of Molecular Morphogenesis, Institute of Animal Physiology and Genetics, Czech Academy of Sciences, Brno, Czech Republic
[2]Department of Experimental Biology, Faculty of Science, Masaryk University, Brno, Czech Republic
[3]Department of Chemistry and Toxicology, Veterinary Research Institute, Brno, Czech Republic
[4]Laboratory of Transgenic Models of Diseases, Institute of Molecular Genetics, Czech Academy of Sciences, Prague, Czech Republic
[5]Czech Centre for Phenogenomics, Institute of Molecular Genetics, Czech Academy of Sciences, Prague, Czech Republic

*Corresponding Author: Marcela Buchtová

Laboratory of Molecular Morphogenesis, Institute of Animal Physiology and Genetics

Czech Academy of Sciences, 602 00 Brno

Czech Republic

Email: buchtova@iach.cz

ORCID ID: 0000-0002-0262-6774

Abstract

Congenital heart defects, facial dysmorphism and intellectual development disorder (CHDFIDD) is associated with mutations in *CDK13* gene, which encodes a transcription regulating Cyclin-dependent kinase 13 (CDK13). Here, we focused on development of craniofacial structures and analyzed early embryonic stages of CHDFIDD mouse models with hypomorphic mutation in *Cdk13* gene, which exhibits cleft lip/palate and knockout of *Cdk13* with stronger phenotype including midfacial cleft. *Cdk13* was found to be physiologically strongly expressed in the mouse embryonic craniofacial structures, namely in the forebrain,

nasal epithelium and maxillary mesenchyme. We also uncovered that *Cdk13*-deficiency leads to development of hypoplastic branches of the trigeminal nerve including maxillary branch and additionally, we detected significant gene expression changes of molecules involved in neurogenesis (*Ache*, *Dcx*, *Mef2c*, *Neurog1*, *Ntn1, Pou4f1*) within the developing palatal shelves. These results, together with changes of gene expression of other key face-specific molecules (*Fgf8, Foxd1*, *Msx1*, *Meis2 and Shh*) at early stages in Cdk13 mutant embryos, demonstrate a key role of CDK13 in regulation of craniofacial morphogenesis.

Keywords: craniofacial development, orofacial clefts, axons, neurite outgrowth, CDK13, trigeminal ganglion

INTRODUCTION

CDK13 is one of the transcriptional kinases, which regulates transcription via phosphorylation of the RNA Polymerase II and controls alternative splicing (Bartkowiak et al., 2010, Blazek et al., 2011). Recently, a few case studies have described a variety of developmental defects in human patients with *CDK13* mutation (Hamilton and Suri, 2019). These patients exhibit delayed development, intellectual disorders, heart and kidney defects and craniofacial deformities. These features have been recognized as Congenital heart defects, facial dysmorphism and intellectual development disorder (CHDFIDD) syndrome. In addition to the most common defects, patients suffer from brain defects, autism, seizures, limb defects, defects in skeletogenesis and other abnormalities (Hamilton and Suri, 2019). To simulate defects presented in patients with *CDK13* mutations, we developed mouse models exhibiting similar phenotype to humans (Nováková et al., 2019). We observed that *Cdk13*-deficiency in the mouse models causes embryonic lethality, delayed development, heart and brain abnormalities and facial phenotype (Nováková et al., 2019).

Here, we performed screening of the *Cdk13* gene expression across the diverse embryonic craniofacial tissues at different developmental stages and evaluated the alteration of developmental processes in craniofacial structures in the *Cdk13*- hypomorph ($Cdk13^{tm1a/tm1a}$) and knock-out ($Cdk13^{tm1d/tm1d}$) mouse embryos with aim to uncover

mechanisms behind observed developmental abnormalities. To determine the modification in molecular regulations caused by *Cdk13*-deficiency, we also analyzed gene expression of patterning molecules involved in craniofacial structures formation.

Moreover, previous *in vitro* approaches uncovered contribution of *Cdk13* mutation to the alteration of neuronal differentiation and neurite outgrowth through regulation of the CDK5 pathway (Chen et al., 2014). These findings are in agreement with observations of neurodevelopmental disorders in human patients bearing *CDK13* mutation (Trinh et al., 2019). Based on this evidence, we focus here on analyses of cranial nerves growth and morphology in *Cdk13*-deficient animals, which are associated with craniofacial structures formation including palate morphogenesis. Further, we evaluated possible changes of neurogenesis specific genes in *Cdk13*-deficient animals and tested the effect of CDK13 inhibitor on axon outgrowth from the embryonic trigeminal ganglion.

RESULTS

Cdk13-deficiency causes craniofacial defects including severe facial clefting

In our previous study, we observed craniofacial developmental defects caused by *Cdk13*-deficiency, which resulted either in a softer phenotype in hypomorphic embryos (secondary palate dysmorphisms at E15.5) or in a stronger phenotype in knock-out embryos (midfacial cleft at E13.5). Morphological difference between these two *Cdk13* genotypes was previously explained by residual expression of the CDK13 in hypomorphic embryos (probably caused by either insertion of neomycin selection cassette in non-coding region that has been shown to affect gene expression, both at the DNA and RNA levels, or high post-transcriptional exon shuffling frequencies in *Cdk13* gene enabling the formation of aberrant functional *Cdk13* transcripts) compared to undetectable CDK13 expression in knock-out embryos (Nováková et al., 2019). Thus, we decided to analyze all the critical stages of $Cdk13^{tm1a/tm1a}$ and $Cdk13^{tmda/tm1d}$ embryos, which exhibited morphological defects of craniofacial structures including severe clefting (Fig.1N).

Split facial prominences and thus widely opened face (midfacial cleft) were detected in E11.5 $Cdk13^{tm1d/tm1d}$ embryos revealing also developing telencephalon in the midline

(Fig.1A´´). At the same stage in *Cdk13*$^{tm1a/tm1a}$ embryos, we detected widely set facial prominences (Fig.1A´). Measurements of distances between individual facial prominences revealed a significantly greater ratio between nasal pits distances and head width in maxillary prominences level and lateral nasal prominences level in both mutant genotypes (Fig.2A-C). Widely set facial prominences in earlier stages progress later at E12.5 to median cleft lip in *Cdk13*$^{tm1a/tm1a}$ embryos (Fig.1B´,H´) but was persisting in *Cdk13*$^{tm1d/tm1d}$ embryos leading to development of midfacial cleft (Fig.1B´´,H´´). Delayed development of the palatal shelves (PSs) (Fig.1E´, K´,K´´) with cleft nasal septum (Fig.1K´,K´´) were detected in both mutant genotypes. Later at E13.5 and E14.5, *Cdk13*$^{tm1a/tm1a}$ embryos displayed thinner lips with wider distance between (Fig.1F´,I´,G´J´) and delayed development of the PSs (Fig.1F´,L´,G´,M´), while *Cdk13*$^{tm1d/tm1d}$ embryos exhibited massive midfacial cleft (Fig.1C´´,I´´,D´´,J´´) and persisting nasal septum cleft (Fig.1L´´,M´´). Less severe defects were detected in the caudal palate area, where underdeveloped PSs were the most prominent feature, especially in *Cdk13*$^{tm1d/tm1d}$ embryos (Fig.S1E-G). At the latest observed stage in E16.5 *Cdk13*$^{tm1a/tm1a}$ embryos, not properly fused lips in the midline together with cleft palate persisted in the rostral and caudal areas accompanied with a necrotic tissue visible in all structures (Fig.S1B-B´´,D,D´). This confirmed embryonic lethality after the stage E15.5, which was noted also previously (Novakova et al. 2019).

Based on craniofacial morphometrics, heads and individual facial prominences are generally smaller in the *Cdk13*-deficient embryos. Thus, we quantified gene expression of the *CyclinD1*, a gene responsible for cell cycle progression from G1 to S phase and used it as a marker of proliferation, to see if there are changes in proliferation rates. *CyclinD1* expression was detected upregulated in almost all the tissues isolated from the E11.5 and E12.5 facial prominences. Although the PSs in the *Cdk13*-deficient animals were generally smaller and exhibited different shape, there were no significant changes detected in *CyclinD1* expression in the PSs of E12.5 *Cdk13*$^{tm1a/tm1a}$ embryos. Slight downregulation was detected in both palatal regions isolated from E14.5 *Cdk13*$^{tm1a/tm1a}$ (Fig.2E). Additional immunostaining of Ki-67 and TUNEL assay confirmed no significant changes in proliferation and apoptosis in the developing palatal shelves of *Cdk13*$^{tm1a/tm1a}$ embryos (Fig.S2A-C).

Expression of *Cdk13* at mRNA level is dispersed through developing facial regions

As we observed distinct changes in facial and palatal morphogenesis in *Cdk13*-deficient embryos, we asked if there is localized expression of the *Cdk13* mRNA to certain areas during craniofacial development. We evaluated gene expression of *Cdk13* on frontal sections to reveal possible differences in its distribution along the labio-lingual axis of the PSs. In E12-E14 embryos, *Cdk13* signal was spread evenly within the palatal mesenchyme and epithelium of the PSs (Fig.3A-C) and later in E15, we detected enriched expression of *Cdk13* in the palatal mesenchyme close to region of fusion in the craniofacial midline (Fig.3D). In the developing snout, intensity of the *Cdk13* signal was similar in the surface epithelium and mesenchyme. Visibly stronger signal was detected in the E11 forebrain (Fig.3F) and nasal epithelium (Fig.3F´´,F´´´) and in the E12 maxillary mesenchyme (Fig.3G). At later stages (E13, E14), *Cdk13* was detected evenly spread in the developing snout in both mesenchyme and epithelium (Fig.S3). Quantification of *Cdk13* expression by qPCR revealed its decreasing level in the palatal area through the development (Fig.3H) and increasing level in the maxillary, mandibular and nasal prominences from E11.5 to E12.5 (Fig.3I).

To uncover possible differences of *Cdk13* distribution along the rostral-caudal axis of the developing palate, we detected its expression on the sagittal sections. In the earlier developmental stages (E11-E14), *Cdk13* was expressed in both rostral and caudal areas of the developing PSs with denser *Cdk13* signal detected in the rostral region compared to caudal areas (Fig.S4A-D; S5). Changes emerged in older embryos (E15-E16), when we observed strong expression of *Cdk13* in the palatal epithelium and adjacent mesenchyme, especially in the developing palatal rugae, both in the rostral and caudal regions (Fig.S4E,F).

CDK13 protein is localized in the cellular outgrowths as well as long neural processes

Next, we asked how CDK13 protein is distributed in cells *in vitro*. We analyzed its expression in cultured MEF cells (mouse embryonic fibroblasts) and cells derived from DRGs (dorsal root ganglia) of adults as these cell types are typical by formation of long cytoplasmic processes.

In MEF cells, the CDK13 was localized in the nuclear area and enriched in cytoplasm around the nucleus (Fig.4A). However, CDK13 protein was also detected in the cellular outgrowths (Fig.4A´-A´´´) including their most apical tips where it was located together with

actin filaments (Fig.4A´). In cells isolated from DRGs, CDK13 was detected in the nuclear area with the strongest expression detected in the cytoplasm closely adjacent to nuclei (Fig.4B). Similarly to MEF cultures, we detected CDK13 in long neural processes along the neurofilaments, which were forming the outgrowths (Fig.4B´,B´´). Documented localization of CDK13 in cytoplasm by immunofluorescence was further evaluated by cellular fractionation followed by western blot of CDK13. As expected, CDK13 was detected in the nuclear fraction of primary MEF cells, but a significant level of CDK13 was also uncovered in the cytoplasmic fraction (Fig.4C). Moreover, the mouse fibroblast cell line NIH3T3 was used to assess subcellular localization of CDK13. The mouse fibroblast cell line NIH3T3 also exhibited presence of CDK13 in both cytoplasmic and nuclear cellular fractions, with higher levels in nuclear fraction (Fig.4D).

Hypomorphic mutation causes production of the truncated form of CDK13 with preserved N-terminal domain (Nováková et al., 2019). This form of CDK13 aggregated in the cellular processes together with deposits of F-actin in E12.5 *Cdk13*$^{tm1a/tm1a}$ MEF (Fig.S6A). Similarly, aggregates of the truncated CDK13 were located in protrusions of cells isolated from E12.5 *Cdk13*$^{tm1a/tm1a}$ DRGs (Fig.S6B). Additionally, live cell imaging on MEF cells revealed different numbers of the cellular protrusions per cell in *Cdk13*$^{tm1d/tm1d}$ cells (Fig.S6C, upper graph) compared to control cells. This was associated with the more stretched morphology of the cultured *Cdk13*$^{tm1d/tm1d}$ cells (Fig.S6D), their weaker adherence to the culture plates and easier release from plates during trypsin digestion (data not shown). On the other hand, cellular velocity (Fig.S6C, lower graph) and the percentage of the cellular surface being protruded (Fig.S6C, middle graph) showed no statistically significant differences between both genotypes in MEF cultures.

This specific cellular localization of the CDK13 to cellular protrusions could indicate a potential cytoplasmic role of the CDK13 protein. However, when we performed detection of ICC signal by polyclonal anti-CDK13 antibodies, we revealed reduction of the CDK13-specific signal in nuclei (arrowheads), but not in the cytoplasm surrounding the nuclei or in the cellular protrusions of *Cdk13*$^{tm1d/tm1d}$ cells (Fig.S6E) indicating primary effect of Cdk13 deficiency on nuclei.

Cdk13-deficiency results in development of hypoplastic cranial nerves

Development of the craniofacial region is closely associated with development of the cranial nerves. A large area is innervated by trigeminal nerve with three main branches: maxillary, mandibular and ophthalmic (Higashiyama and Kuratani, 2014). We detected complex spatial *Cdk13* expression in the developing maxillary nerve (MxN) in cells ensheathing bundles of nerve fibers (Fig.S7A-E´). As the CDK13 was demonstrated to regulate neurite outgrowth (Chen et al., 2014), we hypothesized that alteration of cranial nerves growth could occur during early craniofacial development in *Cdk13*-deficient animals.

First, we visualized outgrowth of cranial nerves by whole mount immunohistochemistry analysis of neurofilaments to uncover possible alterations of general morphology of trigeminal nerve and associated nerves. Alteration of several cranial nerves outgrowth was detected in $Cdk13^{tm1a/tm1a}$ and $Cdk13^{tm1d/tm1d}$ embryos (Fig.5B-C´) with obvious hypoplasia of maxillary (MxN), mandibular (MdN) and ophthalmic (OpN) nerves, which were reduced in length. These nerves originate from the trigeminal ganglion (TG), which we found to be also abridged in the mutant embryos (Fig.5B´,C´). Only the frontal nerve (frN) was not found to be morphologically altered (Fig.B´,C´). This confirms that *Cdk13*-deficiency negatively affects neurogenesis during embryonic development.

Similar to whole mount IHC, changes of nerve protrusions were even more obvious on transversal sections of E11.5 $Cdk13^{tm1d/tm1d}$ embryos. In the rostral region, we observed missing MxN in the developing maxillary prominence (Fig.5D´,E´; Fig.S8A´,B´), hypoplastic MnN in the mandibular prominence (Fig.5E´) and reduced size of the TGs (Fig.S7F,G) confirming defective nerve growth in *Cdk13*-deficient animals.

Changes in expression of key developmental molecules in early craniofacial development of _Cdk13_-deficient embryos

We also detected alterations in expression patterns of genes and proteins strongly associated with craniofacial development and specifically enriched in mesenchymal (SOX9, *Msx1*, *Foxd1*) and epithelial structures (SOX2, *Meis2*, *Shh*) in this region. In E11.5 $Cdk13^{tm1d/tm1d}$ embryos, we observed almost absence of neural crest marker SOX9 in the mesenchyme of lateral nasal prominences (lnp) and maxillary prominences (mx), including area with undeveloped MxN (Fig.5D´; Fig.S8A´). On the other hand, the pattern of SOX2, one

of regulators of neural cells differentiation and peripheral nervous system development (Adameyko et al., 2012), was similar to WT embryos, only missing in the area of the prospective MxN (Fig.5E´; Fig.S8B´). *Meis2*, a gene involved in cranial neural crest development (Machon et al., 2015), was absent from the neural tube in the rostral area (arrow) and less expressed in the same tissue more caudally. Moreover, expression was detected close to facial midline caudally in knockout (asterisk) and not in WT. Conversely, *Meis2* was enriched in the mesenchyme of the rostral medial nasal prominences (Fig.6A). *Msx1*, a key player in craniofacial development (Levi et al., 2006), was absent from the mesenchyme of the medial nasal prominences (asterisks) and also absent from the brain close to its midline (Fig.6B). Detection of genes necessary for determination and development of facial primordia (Jeong et al., 2004), revealed enhanced expression of *Shh* in the ventral neural tube in the rostral region, but similar extend of *Shh* expression in the developing brain more caudally (arrow). Its altered pattern in the epithelium covering forming stomodeal cavity was detected rostrally (Fig.6C). Moreover, enhanced expression of *Shh* downstream gene *Foxd1* in the developing mandibular prominences points also to altered development of the lower jaw (Fig.6D). Finally, *Fgf8* was absent in the epithelium of the developing primitive oral cavity close to the head midline (arrows and asterisks) and its expression was also lower in the developing brain (asterisks), (Fig.6E). It confirms that *Cdk13*-deficiency leads to deregulation of the key developmental genes already in early craniofacial development, which subsequently resulted in severe facial clefting.

Cdk13-deficiency alters expression of neurogenesis-specific genes and key morphogenic molecules in the developing secondary palate

To further evaluate alterations in gene expression of molecules related to neurogenesis during palatogenesis in *Cdk13*$^{tm1a/tm1a}$ embryos, we used PCR Arrays where 84 genes could be analyzed simultaneously. In the separately dissected tissues from rostral and caudal palatal shelves (Fig.7A), we first compared expression of neurogenesis-specific genes between rostral and caudal palatal regions (Table S1-S4).

Out of all the genes in array (Fig.7A), 15 genes (*Ache, Apoe, Bmp2, Dcx, Fgf2, Heyl, Mef2c, Neurod1, Neurog1, Nog, Nrg1, Ntn1, Pou4f1, S100a6, Sox3*) were significantly enriched in caudal PSs compared to rostral PSs when comparing these regions in E12.5

control embryos (Fig.7B, upper left). The same comparison between rostral and caudal PSs in E12.5 *Cdk13*$^{tm1a/tm1a}$ embryos determined preserved gene expression ratio only in case of the *Bmp2* caused probably especially by downregulated expression of caudal PSs-dominant genes (*Ache, Dcx, Ntn1, Pou4f1, Bdnf. Bmp2, Ep300, Fgf2, Heyl, Mef2c, Kmt2a, Neurog1, Nf1, Nog, Notch2, Nrg1, S100a6*) in the caudal PSs (Fig.7C, right). On the contrary, changed ratio was detected in case of *Hey2* and *Ntn1*, whose expression was conversely enriched in the rostral PSs (Fig.7B, upper right) caused by extreme upregulation in mutant embryos (Fig.7C, left).

At later stage in E14.5 control embryos, 10 genes were normally enriched in rostral PSs (*Artn, Bcl2, Bmp2, Gdnf, Hey1, Neurog2, Pax3, Pou3f3, Slit2, Tgfb1*) and 15 genes in caudal PSs (*Ache*, *Apoe, App, Cdk5r1, Dvl3, Fgf2, Map2, Ndn, Nf1, Ntf3, Ntn1, Pafah1b1, Pou4f1, Robo1, Rtn4*), (Fig.7B, lower left). Again, the same comparison between rostral and caudal PSs, this time in E14.5 *Cdk13*$^{tm1a/tm1a}$ embryos, revealed preserved gene expression ratio in 11 genes (*Ache, App, Bcl2, Fgf2, Hey1, Nf1, Ntn1, Pax3, Pou3f3, Slit2 and Tgfb1*) in E14.5 *Cdk13*$^{tm1a/tm1a}$ embryos. Generally, deregulation of the neurogenesis-specific genes in the E14.5 PSs was not so strong (Fig.7D) as was in case of E12.5 (Fig.7C). But, in both observed stages, gene expression was generally downregulated in caudal regions, compared to rostral, where both upregulation and downregulation of gene expression was detected (Fig.7C,D).

Moreover, altered expression of palatal genes and proteins was detected later at E12.5 or E14.5 respectively. *Cdk13*-deficiency leads to noticeable reduction of *Foxd1* in the mesenchyme of snout midline (Fig.7F,G), *Msx1* reduction in the rostral palatal shelves (Fig.7J,K) and also reduction of *Meis2* in the caudal palatal shelves (Fig.7L,M), especially at E12.5. Expression of both SOX9 and SOX2 was similar to the pattern observed in WT animals (Fig.7H,I).

***Cdk13*-deficiency results in changes of RNAPII occupancy within promoters of *Pou4f1* and *Ntn1* genes**

To address the effect of CDK13 depletion on transcription, we performed chromatin immunoprecipitation (ChIP) with a specific antibody recognizing RNA polymerase II (RNAPII) and IgG as a negative control (Fig.S9). We selected two genes from the PCR expression array

(Fig.7), *Pou4f1* and *Ntn1*, for which, we decided to evaluate the presence of RNAPII within their promoter regions in *Cdk13*$^{+/+}$ and *Cdk13*$^{tm1d/tm1d}$ MEF cells. Increased level of RNAPII within both promoters of *Pou4f1* and *Ntn1* was observed in comparison to IgG control (Fig.S9A,B). In the case of the *Pou4f1* promoter, we detected less RNAPII when compared to *Cdk13*$^{+/+}$ MEF cells (Fig.S9A). In contrast, RNAPII was associated more with the promoter of the *Ntn1* gene in *Cdk13*$^{tm1d/tm1d}$ MEFs in comparison to *Cdk13*$^{+/+}$ MEF cells (Fig.S9B). We then decided to compare the presence of RNAPII on these promoters as a percentage of RNAPII compared to IgG control. Faint decrease of RNAPII was observed for *Pou4f1* promoter in *Cdk13*$^{tm1d/tm1d}$ MEF cells in comparison to *Cdk13*$^{+/+}$ MEFs (Fig.S9C). In contrast, the higher occupancy of RNAPII was demonstrated for the *Ntn1* promoter in *Cdk13*$^{tm1d/tm1d}$ MEFs to *Cdk13*$^{+/+}$ MEFs (Fig.S9D). There is no statistical significant difference for RNAPII occupancy at these promoters, nevertheless, obtained observation correlates with decreased and increased mRNA levels of *Pou4f1* and *Ntn1* genes as detected in PCR expression screen (Fig.7), which however will be necessary to follow further.

Chemical inhibition of the CDK13/CDK12 leads to embryonic facial malformations and altered neurite outgrowth

To confirm the effect of CDK13 deactivation on craniofacial structures formation including palatogenesis, we used synthetic CDK13 inhibitor THZ531 to treat early maxillary prominences of the *Gallus gallus* embryos. It is necessary to note that THZ531 is also targeting CDK12, which shares several functions with CDK13 and in developmental processes they can substitute each other under certain conditions. Therefore, the usage of this inhibitor should prevent also compensatory mechanisms induced by CDK13-deficiency.

We injected 1mM THZ531 into the craniofacial mesenchyme at stage HH10, postoptic region at stage HH15 and into maxillary prominences at stage HH20. Then, chicken embryos were allowed to develop for next 4-6 days (Fig.8A). This led to the absence or deficiency of maxillary prominence resulting in the unilateral cleft lip (Fig.8B,C). The application into younger stages resulted in stronger phenotype with large deficiency of mesenchymal cells (Fig. S10).

Furthermore, the effect of *Cdk13*-deficiency on cranial nerves development as shown earlier (Fig.5) was additionally tested by chemical inhibition of CDK13 (together with CDK12)

in functional *ex vivo* cultivation experiment using trigeminal ganglia explants (Fig. 8). TGs were dissected from E12 WT embryos and cultured supplemented with THZ531 inhibitor (100 nM and 300 nM). Significant reduction in formation of neurite outgrowths was observed in TGs when cultured with different concentrations of inhibitor compared to control group (Fig.8E-G) revealing the importance of both CDK13 and CDK12 in development of cranial nerves.

DISCUSSION

CDK13 controls craniofacial morphogenesis through regulation of expression in responsible developmental pathways

Here, we determined a key contribution of CDK13 to the craniofacial morphogenesis and neurogenesis, where the phenotype of *Cdk13*-deficient animals included smaller head and disturbed facial morphology, including facial clefts. In our mutants, we found altered expression patterns of *Msx1*, *Meis2*, *Shh*, *Foxd1* and *Fgf8* in craniofacial structures. Downregulation or upregulation of these genes or their downstream targets causes similar phenotypic craniofacial phenotype including facial clefts or reduced growth of facial nerves (Levi et al., 2006, Machon et al., 2015, Jeong et al., 2004). Pronounced similarities in the morphology of craniofacial structures with the *Cdk13* knockout embryos was previously observed in mice embryos with reduced functional expression levels of *Fgf8.* These animals also exhibited abnormal midline separation with nasal prominences set widely apart (Griffin et al., 2013). Such morphological changes indicate possible insufficiency in development of neural crest cells (NCCs), from which all these affected craniofacial structures are originating and we confirmed it by reduced protein expression of NCC marker SOX9 in facial prominences of *Cdk13*-deficient animals. Moreover, we detected significant downregulation of Mef2c (in all the PSs regions, except rostral E12.5 PSs). Its conditional downregulation specifically in NCCs was previously found to result in craniofacial defects and neonatal lethality (Verzi et al., 2007).

Defects in craniofacial morphogenesis and neurogenesis as a result of disrupted CDK13-associated signaling

Cdk13-deficient mice similarly to patients with mutated *CDK13* or mutations in genes encoding other associated proteins, such as cyclin M, cyclin K, CDK10 (Colas, 2020), and CDK5RAP2 (Yigit et al., 2015) produce neurogenesis defects. These patients exhibit not just craniofacial defects but also affected neural tissues: mutation in *cyclin M* resulted in optic nerve hypoplasia, mutation in *cyclin K* led to developmental delay and intellectual disabilities and mutations in *CDK10* caused intellectual disabilities connected with language and learning disorders. Patients with loss-of-function mutation of *CDK5* displayed craniofacial defects other than facial clefts (short forehead, full cheeks, micrognathia), they also suffer with lissencephaly, cerebellar hypoplasia, microcephaly, intellectual disabilities, speech delay or autistic features (Colas, 2020) similar to patients with *CDK13* mutations (Hamilton and Suri, 2019).

CDK5 has a specific role in neural tissues physiology and regulates several neural processes such as an axonal transport, migration, synaptic vesicle endocytosis and is also important for regulation of axon and neurite outgrowth (Shah and Rossie, 2018). Its knockout leads to perinatal lethality in mice connected with deficient neuronal migration and impaired axonal transport of neurofilaments (Ohshima et al., 1996). Importantly, *in vitro* experiments in cortical neurons demonstrated the role of CDK13 and also CDK12 in regulation of neurite outgrowth through a common signaling pathway that involves modulation of *Cdk5* at the RNA level (Chen et al. 2014). In our *Cdk13*-deficient models, we uncovered significant downregulation of genes encoding CDK5 regulatory subunits, *Cdk5rap2* and *Cdk5r1*, in the E14.5 caudal palatal shelves confirming CDK13-CDK5 functional association observed in *in vitro* experiments. Moreover, *CDK5RAP2* mutations in human patients cause Seckel syndrome manifesting by microcephaly and cognitive problems (Yigit et al., 2015) and *CDK5R1* was proposed as a candidate gene in patients affected by NF1 microdeletion syndrome, which mutations lead to non-syndromic intellectual disability and undefined facial deformities (Venturin et al., 2006).

Inhibitory effect of CDK13 inhibitor THZ531 was demonstrated for the neurite outgrowth from TGs. Even though one could argue that observed effect is result of CDK12 and CDK13 together, it is broadly accepted, that inhibition of CDK12 primarily targets DNA-damage response (DDR) pathway and pre-replication complex assembly (Pilarova et al.,

2020). The process of neurite outgrowth takes place in nondividing differentiated cells of TGs, therefore it is unlikely that altered outgrowth is the result of CDK12 inhibition due to block of cell cycle in S-phase. Also, there is no significant impact of CDK12 inhibition of the DDR pathway since cells with lesser outgrowth of neurites do not exhibit any signs of DDR stress. Thus, documented reduction in neurite outgrowth is likely a result of CDK13 inhibition through a different mechanism, or it could be eventually combinatory effect of CDK12 and CDK13 inhibition through regulation of CDK5 function in neural cytoskeleton organization, which however need further experimental evidence.

Effect of CDK13 on neurogenesis-specific gene expression and cranial nerves development

CDK13 is ubiquitously expressed in murine snout, developing PSs and cranial nerves and its mutation leads to prominent facial clefts. Craniofacial structures, including palate, develop thanks to large contribution of the NCCs. Growing peripheral nerves and glial cell types originate mostly from migrating NCCs and Schwann cell precursors (SCPs) (Furlan and Adameyko, 2018), but there are few exceptions, among them sensory neurons, which innervate maxillary region including the palate. These neurons originate in mesencephalic trigeminal nucleus in CNS and their development is regulated by FGF8 and Pou4f1 (Hunter et al., 2001), in agreement the expression of both genes was detected altered in the *Cdk13*-deficient embryos.

Along with these findings, we detected deregulated expression of genes typically associated with trigeminal ganglion in the developing PSs. *Nrg1* (Meyer et al., 1997), a gene encoding EGF ligand, which in turn induces axon growth (Onesto et al., 2021) was downregulated in E12.5 caudal PSs. Interestingly, also *Nrg1*-deficiency in mice leads to maxillary dysmorphology (Waddington et al., 2017), a structure, from which PSs are developing. Another gene, normally detected in TGs, is *Neurog1,* a neural transcription factor, which was previously associated also with PSs (Visel et al., 2007). Its downregulation in TGs was observed as a result of *Pou4f1* downregulation (Lanier et al., 2009). Similarly, we found *Pou4f1* and *Neurog1* deregulated in E12.5 PSs. But, deregulation of *Neurog1* expression corresponded with expression changes of *Ntn1,* a gene encoding secreted factor responsible for guidance of developing peripheral motor axons (Serafini et al., 1996) and the proposed risk factor for development of the non-syndromic cleft lip and cleft palate (Leslie

et al., 2017). Expression of both genes was highly upregulated in rostral PSs and strongly downregulated in caudal PSs, which in turn exhibits some tendency to rescue growth of nerves to the rostral regions of developing face. Less amount or forming nerves in the facial region of *Cdk13*-deficient embryos is further accompanied with significantly downregulated expression of the *Ache* gene in the E12.5 caudal PSs. *Ache* encodes acetylcholineesterase necessary for the degradation of the acetylcholine leading to the termination of the signal transduction at the neuromuscular junctions, which is also important for neurite outgrowth and its elongation (Olivera et al., 2003).

In *Cdk13*-deficient animals, we also determined alterations in gene expression of molecules involved in neuronal migration, which could lead to altered nerve growth. Such gene, which expression was detected downregulated in all the analyzed PSs regions, is *Pafah1b1*. This gene encodes a protein non-catalytic subunit of an enzyme responsible for activation of GTPases and actin polymerization at the leading edge of locomoting neurons making it important for neural migration (Kholmanskikh et al., 2003). Its mutation in humans frequently results in lissencephaly and Miller-Dieker syndrome (Liu et al., 2021), a disease with very similar phenotypic manifestations compared to patients with the *Cdk13*-deficiency, including growth delay and cerebral, cardiovascular, facial and limb defects (Yingling et al., 2003).

Diverse levels of the Cdk13 action during embryonic development

CDK13 was originally discovered as a nuclear factor participating in the regulation of transcription. We were able to detect CDK13 in the nucleus by immunofluorescence and cellular fractionation, however, we were also able to determine a significant level of CDK13 in the cytoplasm. It might be a rather surprising observation, nevertheless, the presence of CDK13 in the cytoplasm of various cancer cells has been already documented by another group (Wu et al., 2023). Importantly, CDK13 can phosphorylate the intracellular domain of transmembrane protein SERINC5 within the cytoplasm (Chai et al., 2021). These observations indicate that CDK13 can be involved not just in transcription or RNA processing but also in other cellular processes in cytoplasm, which however need further analyses.

Deficiency in cell outgrowths as a potential cause of craniofacial defects

Our findings uncovered that *Cdk13*-deficiency triggers the alteration of neurogenesis-specific genes in the PSs and development of hypoplastic cranial nerves *in vivo* confirming previous *in vitro* study in cortical neurons (Chen et al., 2014). On the other hand, functional connection between defects in cranial nerves development which in turn lead to facial malformations has been detected only in few cases. Such non-canonical function of nerves as moderators of facial morphogenesis has been proven in Möbius syndrome where either defective cranial nerves (Rizos et al., 1998) (Tomas-Roca et al., 2015) or the entire defective rhombencephalon (Verzijl et al., 2003) can cause facial malformations. Another disorders of peripheral nervous system, which lead to facial defects, are hereditary sensory and autonomic neuropathy type IV (HSAN IV) (Gao et al., 2013), (Louryan et al., 1995), (Nakajima et al., 2020) and Parry-Romberg syndrome with Hemifacial atrophy accompanied by various neurological pathologies (Vix et al., 2015). Also downregulated expression of the gene *Nrg1,* which was observed also by us, leads to altered maxillary development (Waddington et al., 2017) as this gene encodes neurogenin ligands with a positive axon growth potential. Nevertheless, functional association between development of hypoplastic peripheral cranial nerves which would lead to development of craniofacial clefts is still missing.

CONCLUSIONS

CDK13 is a key molecule for development of numerous tissues and organs including craniofacial structures. Here, we determined its role during development of facial structures in mouse model of CHDFIDD where loss-of-function in *Cdk13* results in cleft lip/palate and the formation of midfacial cleft accompanied by deregulated expression pattern of major signaling molecules. *Cdk13*-deficient animals exhibited altered neurogenesis accompanied with distorted expression of neurotrophic molecules leading to development of hypoplastic cranial nerves. As our analyses uncovered the cytoplasmic localization of CDK13 in vitro, further investigation is necessary to explore its potential roles beyond transcriptional regulation.

MATERIALS AND METHODS

Embryonic material

Heterozygous hypomorphic (*Cdk13*$^{tm1a(EUCOM)Hmgu}$) and knockout (*Cdk13*^{tm1d}) animals were obtained from the Infrafrontier Research Infrastructure – Mouse disease Models. Mice were generated at the Transgenic and Archiving Module, CCP (IMG, Prague, Czech Republic).

Breeding and genotyping protocols were performed as previously described elsewhere (Nováková et al., 2019) together with the nature of hypomorphic mutation. In summary, *Cdk13*^{tm1a} allele consists of splicing acceptor, which is surrounded by two FRT sites within intron 2. Moreover, it has two lox P sites within intron 2 and one lox P site within intron 4. *Cdk13*^{tm1d} allele bears deletion of exons 3 and 4 resulting in non-functional allele of *Cdk13* gene. *Cdk13*^{tm1a} was described in Novakova et al., 2019.

All animal procedures were performed in strict accordance with the Guide for the Care and Use of Laboratory Animals and approved by the Institutional Animal Care and Use Committee (Masaryk University, Brno, Czechia, No. MSMT-34505/2020-7).

Culture of MEF and NIH3T3 cells

The MEF cells were grown in conventional Dulbecco's modification of Eagle's basal medium (DMEM) culture media supplemented with 4.5 g/L glucose and 20% fetal calf serum, the NIH3T3 cells were grown in DMEM media supplemented with 4.5g/L glucose and 10% fetal calf serum. Cell cultures were maintained on the culture plate at 37°C in 5% CO_2.

Live Cell Imaging

MEF cells isolated from WT and KO embryos were cultured in DMEM medium as explained above. Cells were seeded on ibiTreat µ-Slide 8 Well (80826, Ibidi) in concentration 50000/ml. After the adhesion of cells, medium was changed to Opti-MEM (11058021, Gibco, Thermo Fisher) without phenol red supplemented with 1% fetal bovine serum. Cells were stained with F-actin specific dye and membrane-specific dye 30 minutes prior to the beginning of scanning. Live Imaging was performed using Leica SP8 Confocal microscope (Leica, Germany) equipped with CO_2 and tempered transparent chamber. Further processing and analyses were performed using ImageJ and Adapt plugin for quantification of cell

migration, protrusions, and fluorescence intensities (Barry et al., 2015). Final analysis was performed by GraphPad (GraphPad Software, Boston, MA, USA).

Scanning Electron Microscopy

Embryos (control and *Cdk13*$^{tm1a/tm1a}$) were fixed in 4% paraformaldehyde, washed in distilled water and dehydrated through a graded series (30-100%) of ethanol solutions. Later, samples were dried out using CPD 030 Critical Point Dryer (BAL-TEC) and shadowed by gold in metal shadowing apparatus Balzers SCD040. Samples were observed and photographed in the scanning electron microscope TESCAN Vega TS 5136 XM (Tescan, Czech Republic). SEM was performed on 1 embryo of each stage (E12.5, E13.5, E14.5, E16.5) with representative phenotype.

Measurement of facial proportions

Frontal pictures of E11.5 embryonic heads were snapped using a Leica S6D stereoscope with the DFC295 camera (both Leica, Germany). Individual measurements (mx – distance between edges of the maxillary prominences; lnp – distance between edges of the lateral nasal prominences; pits – distance between individual nasal pits) were performed in AxioVision 4.8 software (Zeiss, Germany) using length measurement tool. Ratios between distances were calculated as follows: *distance between nasal pits/distance mx*, and *distance between nasal pits/distance lnp*. Graphs and statistical significance were performed in GraphPad (GraphPad Software, Boston, MA, USA). Measurements were performed in at least 4 different embryos of all three genotypes (*Cdk13*$^{+/+}$, *Cdk13*$^{tm1a/tm1a}$ and *Cdk13*$^{tm1d/tm1d}$).

Immunofluorescence on slides

Embryonic tissues were fixed in 4% PFA overnight. Specimens were then embedded in paraffin and cut in transverse and sagittal planes for 5 µm sections. For immunohistochemistry staining, sections were deparaffinized in xylen and rehydrated in an ethanol series. Antigen retrieval was performed either in 1% citrate buffer or in DAKO antigen retrieval solution (S1699, DAKO Agilent, USA) at 97.5 ^{o}C.

For protein localization, we incubated sections with primary antibody (Table S5) for 1 hour at room temperature or overnight at 4 °C. Following antibodies were used: 2H3 (1:50, Nefm, AB_2314897, Developmental Studies Hybridoma Bank), SOX2 (1:100, 2748s, Cell Signaling), SOX9 (1:100, HPA001758, Sigma), Ki67 (1:200, RBK027, Zytomed systems). Then sections were incubated with the following secondary antibodies (1:200) for 30 minutes at room temperature: anti-mouse Alexa Fluor 488 (A11001), and anti-rabbit Alexa Fluor 594 (A11037, both Thermo Fisher Scientific, USA). Ki-67 positive cells were detected by anti-rabbit secondary antibody, ABC binding (PK-6101, Vector laboratories) and followed by application of the DAB (K3468, Dako) chromogenic system.

Sections were mounted with Fluoroshield with DAPI (F6057, Sigma, Merck, Germany). If DRAQ5 (62251, Thermo Fisher Scientific, USA) was used for nuclei staining, sections were mounted with Fluoroshield (F6182, Sigma, Merck, Germany). Pictures were taken on confocal microscopes Leica SP8 (Leica, Germany) and Zeiss LSM800 (Zeiss, Germany). Nuclei on DAB stained sections were counterstained with hematoxilyn. Sections were photographed under bright-field illumination with the Leica DMLB2 compound microscope (Leica, Germany).

Mitotic index on Ki-67 stained sections in the palatal shelves, was counted as a ratio between Ki-67-positive cells (brown) and total number of cells (negative plus Ki-67- positive cells). Cells were counted independently in mesenchyme and epithelium of the palatal shelves. Cells were counted on 4 sections (both left and right palatal shelves) in 3 embryos for each genotype (*Cdk13*$^{+/+}$ and *Cdk13*$^{tm1a/tm1a}$).

Immunocytochemistry on glass inserts

Mesenchymal embryonic fibroblasts (MEF) and cells from embryonic DRGs (dorsal root ganglia) were isolated from E12.5 embryonic bodies. Tissues were enzymatically processed using Dispase II (D4693, Sigma, Merck, Germany) for 1 hour at 37 °C while shaking. Cells were then centrifuged, filtered through 40 µm Cell strainer (431750, Corning), seeded on glass inserts and left to grow until 70 – 80 % confluency in DMEM cultivation medium (D6546, Sigma, Merck, Germany). Adult DRG cells were isolated from DRGs from adult mice. DRGs were enzymatically processed using Collagenase IV (LS0004188, PAN Biotech) for 6 hours at 37 °C. Tissues were resuspended every hour by pipetting. Cells were

then filtered through Cell strainer and seeded on glass inserts and left to grow and form long outgrowths in Neurobasal cultivation medium (21103-49, Gibco). Cells were then fixed in 4% PFA for 15 minutes.

For protein localization, we incubated cells on glass inserts with primary antibody for 1 hour at room temperature. Following antibodies were used: anti-CDK13 (1:100, HPA059241, Sigma, Merck, Germany), anti-CDK13 N-TERM (1:100, SAB1302350, Sigma), anti-CDK13 (1:150, PA5-63692, Invitrogen, Thermo Fisher Scientific, USA), anti-F-actin (1:100, A12379, Alexa Fluor 488™ phalloidin, Thermo Fisher), anti-2H3 (1:50, Nefm, AB_2314897, Developmental Studies Hybridoma Bank). Then sections were incubated with the following secondary antibodies (1:200) for 30 minutes at room temperature: anti-mouse Alexa Fluor 488 (A11001), and anti-rabbit Alexa Fluor 594 (A11037, both Thermo Fisher Scientific, USA). Glass inserts were mounted on glass slides with Fluoroshield with DAPI (F6057, Sigma, Merck, Germany). Pictures were taken on confocal microscope Leica SP8 (Leica, Germany). Cells were cultivated from at least 3 different embryos of all three genotypes (*Cdk13*$^{+/+}$, *Cdk13*$^{tm1a/tm1a}$ and *Cdk13*$^{tm1d/tm1d}$).

Whole mount immunofluorescence

Embryos were dissected, fixed in 4% PFA while rotating at 4 ^{o}C for 4 hours. Embryos were then postfixed in methanol through gradual concentrations of methanol (25%, 50%, 75%, 100%). Embryos were then bleached in a mixture of hydrogen peroxide, DMSO and methanol for 24 hours and then postfixed in combination of DMSO and methanol. Embryos were incubated with primary antibody to neurofilaments (2H3, AB_2314897, Developmental Studies Hybridoma Bank) for 7 days while rotating and then with secondary antibody (anti-mouse Alexa Fluor 488, A11001) for 2 days while rotating. Embryos were finally cleared in a mixture of benzyl benzoate and benzyl alcohol until they got transparent. For microscopy, we placed embryos on NuncTM Glass Bottom dish (150680, Thermo Fisher) and imaged them on Zeiss AxioZoom.V16-Apotome2 (Zeiss, Germany) at CELLIM (Core Facility Cellular Imaging, CEITEC, Masaryk University, Brno, Czech Republic). Whole mount immunodetection of the neurofilaments was performed in 3 different embryos of all three genotypes (*Cdk13*$^{+/+}$, *Cdk13*$^{tm1a/tm1a}$ and *Cdk13*$^{tm1d/tm1d}$) at E11.5 stage.

Cellular Fractionation

MEF and MIH3T3 cells were cultured on a 100 mm culture plate until 75% confluent in a 37°C incubator supplied with 5% CO_2. Cells were washed with ice-cold PBS and collected into 1 ml of ice-cold PBS with a scraper and transferred to the 1,5 ml Eppendorf tube. Centrifugation for 4 min, 300xg, 4^{o}C. Pellet of cells was resuspended in 200 µl of TMK buffer (25 mM Tris-HCl, pH=7,4; 5 mM KCl; 1 mM $MgCl_2$) and additional 150 µl of TMK+1% NP-40 was added to the tube. Incubation on ice for 5 min followed by centrifugation for 5 min, 250xg, 4^{o}C. Supernatant (cytoplasmic fraction) was transferred to the new 1,5 ml Eppendorf tube. Pellet (nuclei) was resuspended in 500 µl of buffer S1 (0,25 M Saccharose; 10 mM $MgCl_2$) and transferred to the new Eppendorf tube on top of 500 µl of buffer S2 (0,35 M Saccharose; 0,5 mM $MgCl_2$), followed by centrifugation for 5 min, 1400xg, 4^{o}C. Supernatant was removed and the pellet was resuspended in 50 µl of ice-cold PBS. Protein concentration was assessed for cytoplasmic and nuclear samples and an appropriate volume of 3xLaemmli buffer was added to the given samples. The samples were boiled for 5 min at 100 ^{o}C, followed by western blot procedure as published in (Blazek et al., 2011). Antibodies used in western blot CDK13 (Merck, cat.n.: HPA059241), PARP (Cell Signaling Technology, cat.n.: 9542S), α-Tubulin (Cell Signaling Technology, cat.n.: 7291S), Lamin B (Santa Cruz Technology, cat.n.: sc-6217) and GAPDH (Santa Cruz Technology, cat.n.: sc-23233).

Chromatin immunoprecipitation (ChIP)

The same chromatin immunoprecipitation protocol was employed as published by Blažek et al. with few modifications (Blazek et al., 2011). MEF cells were washed with PBS and cross-linked with 1% formaldehyde/PBS solution for 10 minutes at room temperature. The cross-linking was quenched for 5 minutes with 125 mM Glycine (final concentration). Cells were washed twice with ice cold PBS and lysed in sonication buffer (0.5% SDS, 20 mM Tris-HCl pH=8.0, 2 mM EDTA, 0.5 mM EGTA, 0.5 mM PMSF, protease inhibitor. For immunoprecipitation protein extract was pre-cleared with ChIP Grade G Agarose Beads (Cell Signaling Technology, cat.n.: 9007S) and then incubated overnight with RNAPII antibody (Cell Signaling Technology, Rpb1 NTD (D8L4Y), cat.n.: 14958S), followed by 2 hours incubation with ChIP Grade G Agarose Beads. The Beads were washed once with low salt buffer 0.1% SDS, 1% TritonX-100, 2 mM EDTA, 20 mM Tris-HCl pH=8.0, 150 mM NaCl followed by the

triple wash with the same buffer containing 500 mM NaCl and one wash with lithium buffer (2 mM EDTA, 20 mM Tris pH=8, 250 mM LiCl, 1% NP-40 and 1% natrium deoxycholate) and two washes with TE buffer. We eluted the immunoprecipitate with 1% SDS and 100 mM natrium bicarbonate at room temperature for 15 minutes and cross-linking was reversed with 200 mM NaCl for 5 hours at 65 °C. Proteins were digested with Proteinase K (Sigma) and DNA extracted with phenol/chloroform/isoamyl alcohol (25:24:1) extraction and precipitated with isopropanol overnight. A fraction of precipitated DNA was used in qPCR reactions with the KAPA SYBR FAST qPCR Master Mix (2X) optimized for LightCycler® 480 (Merck, KK4611). The amplifications were run on the Roche LC480II using the following conditions: initial activation step at 94°C for 5 min, followed by 45 cycles at 95 °C for 10s, 60°C for 20 s and 72°C for 15s. For the promoter of *Pou4f1* gene the primers Fw: AGAAATGCGCTGTGGATGAT and Re: TCCCGAGTAGAAAGCACACA were used from the publication (Tang et al., 2020). For the promoter of *Ntn1* gene the primers Fw: GTCGGCAAATTTTCTCCAAA and Re: GTTGCATCCTTTCACCCACT were used from the publication (Kaneko et al., 2014).

PCR arrays analysis

PCR arrays were performed on tissues isolated from rostral and caudal parts of the palatal shelves from E12.5 and E14.5 embryos. One sample was pooled from two or three embryos, three biological replicates for each stage and genotype were analyzed. Total RNA was extracted using RNeasy Plus Mini Kit (74136, Qiagen, Germany) according to the manufacturer`s instructions. Total RNA concentration and purity was measured using a NanoDrop One (Thermo Fisher Scientific, USA). First-strand cDNA was synthesized using gb Reverse Transcription Kit (3012, Generi Biotech, Czech Republic) according to the manufacturer`s instructions. RT² Profiler™ PCR Array Mouse Neurogenesis (330231, Qiagen, Germany) was performed according to the manufacturer`s instructions on LightCycler 96 (Roche, Germany). C_T values were exported to an Excel file to create a table of C_T values. This table was then uploaded on to the data analysis web portal at http://www.qiagen.com/geneglobe. Samples were assigned to controls and test groups. C_T values were normalized to *Gapdh* reference gene. The data analysis web portal calculates fold change/regulation using delta delta C_T method, in which delta C_T is calculated between

gene of interest (GOI) and an average of reference genes (HKG), followed by delta-delta C_T calculations (delta C_T (Test Group)-delta C_T (Control Group)). Fold Change is then calculated using 2^ (-delta delta C_T) formula. The p values are calculated based on a Student's t-test of the replicate 2^(- Delta C_T) values for each gene in the control group and test groups. The p-value calculation used is based on parametric, unpaired, two-sample equal variance, two-tailed distribution.

RNAScope

The embryos were fixed in 4% PFA and fixation time differed based on the stage. The tissues were then dehydrated in an ethanol series, embedded in paraffin, and 5 µm transverse sections were obtained. The sections were deparaffinized in xylene and dehydrated in 100% ethanol. To detect gene expression, we used the RNAScope Multiplex Fluorescent v2 Assay kit (323 110, ACD Bio, United States) for formalin-fixed paraffin embedded tissues according to the manufacturer's instructions. All reactions, which require 40 ^{o}C incubation temperature, were performed in the HybEZTM II Oven (ACD Bio, United States). Probes for *Cdk13* (895581), *Fgf8* (313411), *FoxD1* (495501), *Meis2* (436371), *Msx1* (421841) and *Shh* (314361), all ACD Bio, United States, were used. For negative control staining, a probe diluent (300041) was used instead of a probe. The hybridized probes were visualized using the TSA-Plus Cyanine 3 system (NEL744001KT, Perkin-Elmer, United States), according to the manufacturer's protocol. DAPI (323 108, ACD Bio, United States) was used to stain nuclei. Pictures were obtained with the Leica SP8 confocal microscope (Leica, Germany).

RNAscope® Probe Mm-*Cdk13* (#895581) binds to nucleotides 3312 to 4317 of NM_001081058.2 (last couple of exons and the 3'UTR). If the deletion of exons 3 and 4 (*Cdk13*$^{tm1d/tm1d}$) is not stable, there is possibility to have a signal (some weak signal in the form of dots is present in both hypomorphic and knock-out embryonic palatal shelves).

RT-PCR

Rostral and caudal parts of the palatal shelves (E12.5, E14.5, E16.5), and maxillary (mx), mandibular (md) and frontonasal prominences (fnp) (E11.5, E12.5) from WT embryos

were dissected to quantify differences in *Cdk13* expression during development of the facial structures. Individual parts of the palatal shelves and facial prominences were dissected from at least 3 different embryos for each stage. Proliferation rate changes in the *Cdk13*-deficient embryos were assessed using *CyclinD1* gene expression in tissues isolated from the rostral and caudal palatal shelves (*Cdk13*^{tm1a} E12.5, E14.5) and from lips (*Cdk13*^{tm1d} E12.5). Total RNA was extracted using RNeasy Plus Mini Kit (74136, Qiagen, Germany) according to the manufacturer's instructions. Total RNA concentration and purity was measured using a NanoDrop One (Thermo Fisher Scientific, USA). First-strand cDNA was synthesized using gb Reverse Transcription Kit (3012, Generi Biotech, Czech Republic) according to the manufacturer's instructions. TaqMan probe was used to quantify *Cdk13* (Mm01164725_m1, Thermo Fisher) and *CyclinD1* (Mm00432359_m1, Thermo Fisher) gene expression. The RT-PCR reaction was performed on LightCycler 96 (Roche, Germany). The comparative C_T method was used for analysis.

Chicken embryo injections

Fertilized eggs (*Gallus gallus*) were bought at the farm (Integra, Zabcice, Czech Republic) and incubated in a humidified incubator at 37 ^{O}C. At developmental stage HH20, 1mM THZ531 CDK12/13 inhibitor (SML, 2619, Sigma Aldrich, Merck, Germany) was injected into the maxillary prominences (Fig. 9) using glass capillary attached to EppendorfTM FemtoJetTM 4i Microinjector (Eppendorf, Germany) supplied with a manipulator (Leica, Germany). Moreover, we injected inhibitor to the craniofacial mesenchyme at stage HH10 and postoptic region ate stage HH15 (Fig. 9). 10% Trypan blue was used as a contrasting dye. After injections, chicks were incubated for another 96 hours and then sacrificed and fixed in 4% paraformaldehyde. Frontal and lateral pictures were snapped using a Leica S6D stereoscope with the DFC295 camera (both Leica, Germany).

MTT-Assay

The MTT test was used for the establishment of THZ531 inhibitor toxicity. Cells isolated from TGs were cultivated for 4 days in 100 µl of the medium in a 96-well plate (100 000 cells/ml). Cells were treated every day with different concentrations of the THZ531

inhibitor (50, 100, 300, 500, 750, 1000 and 1500 nM). Untreated cells were used as controls. The medium was discarded and replaced with 50 µl of medium not containing FBS and 50 µl of MTT Reagent (MTT Cell Proliferation Kit Ab211091, Abcam). 50 µl of common culture medium and 50 µl of MTT Reagent was also added to empty wells and used as background controls. The plate was incubated in foil for 3.5 hours at 37 °C 5% CO2. Afterward, 150 µl of MTT Solvent (MTT Cell Proliferation Kit Ab211091, Abcam) was added to the samples. Finally, the absorbance was measured at 590 nm. Cell survival rate was established as an absorbance index (higher absorbance - better cell survival; lower absorbance - worse cell survival), (Fig.S7H).

Trigeminal ganglia cultivation and neurite outgrowth assay

Trigeminal ganglia were dissected from E12 embryos and washed in ice cold Neurobasal medium. Each TG was placed in a separate well on a culture well plate into 10 µl drop of Matrigel (356231, Corning, USA) and left 20 minutes to polymerize in the tissue culture incubator. Neurobasal medium (21103049, Gibco, Thermo Fisher, USA) supplemented with 100 nM or 300 nM THZ531 inhibitor (SML2619, Sigma Aldrich, Merck, Germany) was added. Pictures were snapped after adding cultivation medium (0 h) and then after 24 hours using Olympus IX71 inverted microscope (Olympus, Japan). Neurite outgrowth was measured using ImageJ software (NIH, USA) while comparing areas covered by neurites on pictures of different culture conditions. Percentage changes in ability of TGs to produce neurite outgrowths were calculated as following: *neurite outgrowth area (total area – TG area)/total area*100*.

Terminal Deoxynucleotidyl Transferase dUTP Nick End Labeling (TUNEL) Assay

Apoptotic cells were detected using the TUNEL assay (ApopTag Peroxidase In Situ Apoptosis Detection Kit, Cat. No. S7101, Chemicon, Temecula, United States). Nuclei were counterstained with Hematoxylin. Sections were photographed under bright-field illumination with the Leica DMLB2 compound microscope (Leica, Germany). TUNEL Assay was performed in 3 different embryos of *Cdk13*$^{+/+}$ and *Cdk13*$^{tm1a/tm1a}$ genotypes.

Statistical analyses

Data were evaluated for statistical significance in GraphPad (GraphPad Software, Boston, MA, USA) using unpaired two-tailed Student's t-tests. Differences were considered to be significant at $p<0.05$, $p<0.01$ and $p<0.001$ and were indicated by *, ** or *** symbols, respectively.

ACKNOWLEDGEMENT

This work was supported by the Czech Science Foundation (19-01205S, 22-02794S), by the MEYS CR (CZ.02.1.01/0.0/0.0/15_003/0000460) and by the National Institute for Cancer Research (Programme EXCELES, ID Project No. LX22NPO5102) - Funded by the European Union - Next Generation EU. We acknowledge the core facility CELLIM supported by the Czech-BioImaging large RI project (LM2018129 funded by MEYS CR).

Conflicts of interest

The authors declare no potential conflicts of interest with respect to the authorship and/or publication of this article.

Author contributions

M. Hampl, contributed to conception and design, data acquisition, analysis, and interpretation, drafted the manuscript; N. Jandova, contributed to data acquisition, analysis, and interpretation, critically revised the manuscript; M. Novakova, J Kohoutek contributed to data acquisition, analysis and interpretation; Denisa Lusková, Tereza Szotkowska and Stepan Cada contributed to data acquisition and analyses, J. Prochazka and M. Buchtova, contributed to conception and design, critically revised the manuscript. All authors gave final approval and agree to be accountable for all aspects of the work.

REFERENCES

ADAMEYKO, I., LALLEMEND, F., FURLAN, A., ZININ, N., ARANDA, S., KITAMBI, S. S., BLANCHART, A., FAVARO, R., NICOLIS, S., LÜBKE, M., MÜLLER, T., BIRCHMEIER, C., SUTER, U., ZAITOUN, I., TAKAHASHI, Y. & ERNFORS, P. 2012. Sox2 and Mitf cross-regulatory interactions consolidate progenitor and melanocyte lineages in the cranial neural crest. *Development,* 139**,** 397-410.

BAI, J., RAMOS, R. L., PARAMASIVAM, M., SIDDIQI, F., ACKMAN, J. B. & LOTURCO, J. J. 2008. The role of DCX and LIS1 in migration through the lateral cortical stream of developing forebrain. *Dev Neurosci,* 30**,** 144-56.

BARRY, D. J., DURKIN, C. H., ABELLA, J. V. & WAY, M. 2015. Open source software for quantification of cell migration, protrusions, and fluorescence intensities. *J Cell Biol,* 209**,** 163-80.

BARTKOWIAK, B., LIU, P., PHATNANI, H. P., FUDA, N. J., COOPER, J. J., PRICE, D. H., ADELMAN, K., LIS, J. T. & GREENLEAF, A. L. 2010. CDK12 is a transcription elongation-associated CTD kinase, the metazoan ortholog of yeast Ctk1. *Genes Dev,* 24**,** 2303-16.

BLAZEK, D., KOHOUTEK, J., BARTHOLOMEEUSEN, K., JOHANSEN, E., HULINKOVA, P., LUO, Z., CIMERMANCIC, P., ULE, J. & PETERLIN, B. M. 2011. The Cyclin K/Cdk12 complex maintains genomic stability via regulation of expression of DNA damage response genes. *Genes Dev,* 25**,** 2158-72.

CHAI, Q., LI, S., COLLINS, M. K., LI, R., AHMAD, I., JOHNSON, S. F., FRABUTT, D. A., YANG, Z., SHEN, X., SUN, L., HU, J., HULTQUIST, J. F., PETERLIN, B. M. & ZHENG, Y. H. 2021. HIV-1 Nef interacts with the cyclin K/CDK13 complex to antagonize SERINC5 for optimal viral infectivity. *Cell Rep,* 36**,** 109514.

CHAN, H. M. & LA THANGUE, N. B. 2001. p300/CBP proteins: HATs for transcriptional bridges and scaffolds. *J Cell Sci,* 114**,** 2363-73.

CHEN, H. R., LIN, G. T., HUANG, C. K. & FANN, M. J. 2014. Cdk12 and Cdk13 regulate axonal elongation through a common signaling pathway that modulates Cdk5 expression. *Exp Neurol,* 261**,** 10-21.

COLAS, P. 2020. Cyclin-dependent kinases and rare developmental disorders. *Orphanet J Rare Dis,* 15**,** 203.

FRIOCOURT, G., KOULAKOFF, A., CHAFEY, P., BOUCHER, D., FAUCHEREAU, F., CHELLY, J. & FRANCIS, F. 2003. Doublecortin functions at the extremities of growing neuronal processes. *Cereb Cortex,* 13**,** 620-6.

FURLAN, A. & ADAMEYKO, I. 2018. Schwann cell precursor: a neural crest cell in disguise? *Dev Biol,* 444 Suppl 1**,** S25-S35.

GAO, L., GUO, H., YE, N., BAI, Y., LIU, X., YU, P., XUE, Y., MA, S., WEI, K., JIN, Y., WEN, L. & XUAN, K. 2013. Oral and craniofacial manifestations and two novel missense mutations of the NTRK1 gene identified in the patient with congenital insensitivity to pain with anhidrosis. *PLoS One,* 8**,** e66863.

GRIFFIN, J. N., COMPAGNUCCI, C., HU, D., FISH, J., KLEIN, O., MARCUCIO, R. & DEPEW, M. J. 2013. Fgf8 dosage determines midfacial integration and polarity within the nasal and optic capsules. *Dev Biol,* 374**,** 185-97.

HAMILTON, M. J. & SURI, M. 2019. CDK13-related disorder. *Adv Genet,* 103**,** 163-182.

HIGASHIYAMA, H. & KURATANI, S. 2014. On the maxillary nerve. *J Morphol,* 275**,** 17-38.

HUNTER, E., BEGBIE, J., MASON, I. & GRAHAM, A. 2001. Early development of the mesencephalic trigeminal nucleus. *Dev Dyn,* 222**,** 484-93.

JEONG, J., MAO, J., TENZEN, T., KOTTMANN, A. H. & MCMAHON, A. P. 2004. Hedgehog signaling in the neural crest cells regulates the patterning and growth of facial primordia. *Genes Dev,* 18**,** 937-51.

KANEKO, S., SON, J., BONASIO, R., SHEN, S. S. & REINBERG, D. 2014. Nascent RNA interaction keeps PRC2 activity poised and in check. *Genes Dev,* 28**,** 1983-8.

KAPPELER, C., SAILLOUR, Y., BAUDOIN, J. P., TUY, F. P., ALVAREZ, C., HOUBRON, C., GASPAR, P., HAMARD, G., CHELLY, J., MÉTIN, C. & FRANCIS, F. 2006. Branching and nucleokinesis defects in migrating interneurons derived from doublecortin knockout mice. *Hum Mol Genet,* 15**,** 1387-400.

KHOLMANSKIKH, S. S., DOBRIN, J. S., WYNSHAW-BORIS, A., LETOURNEAU, P. C. & ROSS, M. E. 2003. Disregulated RhoGTPases and actin cytoskeleton contribute to the migration defect in Lis1-deficient neurons. *J Neurosci,* 23**,** 8673-81.

LANIER, J., DYKES, I. M., NISSEN, S., ENG, S. R. & TURNER, E. E. 2009. Brn3a regulates the transition from neurogenesis to terminal differentiation and represses non-neural gene expression in the trigeminal ganglion. *Dev Dyn,* 238**,** 3065-79.

LESLIE, E. J., CARLSON, J. C., SHAFFER, J. R., BUTALI, A., BUXÓ, C. J., CASTILLA, E. E., CHRISTENSEN, K., DELEYIANNIS, F. W., LEIGH FIELD, L., HECHT, J. T., MORENO, L., ORIOLI, I. M., PADILLA, C., VIEIRA, A. R., WEHBY, G. L., FEINGOLD, E., WEINBERG, S. M., MURRAY, J. C., BEATY, T. H. & MARAZITA, M. L. 2017. Genome-wide meta-analyses of nonsyndromic orofacial clefts identify novel associations between FOXE1 and all orofacial clefts, and TP63 and cleft lip with or without cleft palate. *Hum Genet,* 136**,** 275-286.

LEVI, G., MANTERO, S., BARBIERI, O., CANTATORE, D., PALEARI, L., BEVERDAM, A., GENOVA, F., ROBERT, B. & MERLO, G. R. 2006. Msx1 and Dlx5 act independently in development of craniofacial skeleton, but converge on the regulation of Bmp signaling in palate formation. *Mech Dev,* 123**,** 3-16.

LIU, X., BENNISON, S. A., ROBINSON, L. & TOYO-OKA, K. 2021. Responsible Genes for Neuronal Migration in the Chromosome 17p13.3: Beyond. *Brain Sci,* 12.

LOURYAN, S., BIERMANS, J. & FLEMAL, F. 1995. Nerve growth factor in the developing craniofacial region of the mouse embryo. *Eur J Morphol,* 33**,** 415-9.

MACHON, O., MASEK, J., MACHONOVA, O., KRAUSS, S. & KOZMIK, Z. 2015. Meis2 is essential for cranial and cardiac neural crest development. *BMC Dev Biol,* 15**,** 40.

MEYER, D., YAMAAI, T., GARRATT, A., RIETHMACHER-SONNENBERG, E., KANE, D., THEILL, L. E. & BIRCHMEIER, C. 1997. Isoform-specific expression and function of neuregulin. *Development,* 124**,** 3575-86.

NAKAJIMA, K., MIRANDA, A., CRAIG, D. W., SHEKHTMAN, T., KMOCH, S., BLEYER, A., SZELINGER, S., KATO, T. & KELSOE, J. R. 2020. Ntrk1 mutation co-segregating with bipolar disorder and inherited kidney disease in a multiplex family causes defects in neuronal growth and depression-like behavior in mice. *Transl Psychiatry,* 10**,** 407.

NOVÁKOVÁ, M., HAMPL, M., VRÁBEL, D., PROCHÁZKA, J., PETREZSELYOVÁ, S., PROCHÁZKOVÁ, M., SEDLÁČEK, R., KAVKOVÁ, M., ZIKMUND, T., KAISER, J., JUAN, H. C., FANN, M. J., BUCHTOVÁ, M. & KOHOUTEK, J. 2019. Mouse Model of Congenital Heart Defects, Dysmorphic Facial Features and Intellectual Developmental Disorders as a Result of Non-functional CDK13. *Front Cell Dev Biol,* 7**,** 155.

OHSHIMA, T., WARD, J. M., HUH, C. G., LONGENECKER, G., VEERANNA, PANT, H. C., BRADY, R. O., MARTIN, L. J. & KULKARNI, A. B. 1996. Targeted disruption of the cyclin-dependent kinase 5 gene results in abnormal corticogenesis, neuronal pathology and perinatal death. *Proc Natl Acad Sci U S A,* 93**,** 11173-8.

OLIVERA, S., RODRIGUEZ-ITHURRALDE, D. & HENLEY, J. M. 2003. Acetylcholinesterase promotes neurite elongation, synapse formation, and surface expression of AMPA receptors in hippocampal neurones. *Mol Cell Neurosci,* 23**,** 96-106.

ONESTO, M. M., SHORT, C. A., REMPEL, S. K., CATLETT, T. S. & GOMEZ, T. M. 2021. Growth Factors as Axon Guidance Molecules: Lessons From. *Front Neurosci,* 15**,** 678454.

PILAROVA, K., HERUDEK, J. & BLAZEK, D. 2020. CDK12: cellular functions and therapeutic potential of versatile player in cancer. *NAR Cancer,* 2**,** zcaa003.

RIZOS, M., NEGRÓN, R. J. & SERMAN, N. 1998. Möbius syndrome with dental involvement: a case report and literature review. *Cleft Palate Craniofac J,* 35**,** 262-8.

SERAFINI, T., COLAMARINO, S. A., LEONARDO, E. D., WANG, H., BEDDINGTON, R., SKARNES, W. C. & TESSIER-LAVIGNE, M. 1996. Netrin-1 is required for commissural axon guidance in the developing vertebrate nervous system. *Cell,* 87**,** 1001-14.

SHAH, K. & ROSSIE, S. 2018. Tale of the Good and the Bad Cdk5: Remodeling of the Actin Cytoskeleton in the Brain. *Mol Neurobiol,* 55**,** 3426-3438.

TANG, P. M., ZHANG, Y. Y., XIAO, J., TANG, P. C., CHUNG, J. Y., LI, J., XUE, V. W., HUANG, X. R., CHONG, C. C., NG, C. F., LEE, T. L., TO, K. F., NIKOLIC-PATERSON, D. J. & LAN, H. Y. 2020. Neural transcription factor Pou4f1 promotes renal fibrosis via macrophage-myofibroblast transition. *Proc Natl Acad Sci U S A,* 117**,** 20741-20752.

TOMAS-ROCA, L., TSAALBI-SHTYLIK, A., JANSEN, J. G., SINGH, M. K., EPSTEIN, J. A., ALTUNOGLU, U., VERZIJL, H., SORIA, L., VAN BEUSEKOM, E., ROSCIOLI, T., IQBAL, Z., GILISSEN, C., HOISCHEN, A., DE BROUWER, A. P. M., ERASMUS, C., SCHUBERT, D., BRUNNER, H., PÉREZ AYTÉS, A., MARIN, F., AROCA, P., KAYSERILI, H., CARTA, A., DE WIND, N., PADBERG, G. W. & VAN BOKHOVEN, H. 2015. De novo mutations in PLXND1 and REV3L cause Möbius syndrome. *Nat Commun,* 6**,** 7199.

TRINH, J., KANDASWAMY, K. K., WERBER, M., WEISS, M. E. R., OPREA, G., KISHORE, S., LOHMANN, K. & ROLFS, A. 2019. Novel pathogenic variants and multiple molecular diagnoses in neurodevelopmental disorders. *J Neurodev Disord,* 11**,** 11.

VENTURIN, M., MONCINI, S., VILLA, V., RUSSO, S., BONATI, M. T., LARIZZA, L. & RIVA, P. 2006. Mutations and novel polymorphisms in coding regions and UTRs of CDK5R1 and OMG genes in patients with non-syndromic mental retardation. *Neurogenetics,* 7**,** 59-66.

VERZI, M. P., AGARWAL, P., BROWN, C., MCCULLEY, D. J., SCHWARZ, J. J. & BLACK, B. L. 2007. The transcription factor MEF2C is required for craniofacial development. *Dev Cell,* 12**,** 645-52.

VERZIJL, H. T., VAN DER ZWAAG, B., CRUYSBERG, J. R. & PADBERG, G. W. 2003. Möbius syndrome redefined: a syndrome of rhombencephalic maldevelopment. *Neurology,* 61**,** 327-33.

VISEL, A., CARSON, J., OLDEKAMP, J., WARNECKE, M., JAKUBCAKOVA, V., ZHOU, X., SHAW, C. A., ALVAREZ-BOLADO, G. & EICHELE, G. 2007. Regulatory pathway analysis by high-throughput in situ hybridization. *PLoS Genet,* 3**,** 1867-83.

VIX, J., MATHIS, S., LACOSTE, M., GUILLEVIN, R. & NEAU, J. P. 2015. Neurological Manifestations in Parry-Romberg Syndrome: 2 Case Reports. *Medicine (Baltimore),* 94**,** e1147.

WADDINGTON, J. L., KATINA, S., O'TUATHAIGH, C. M. P. & BOWMAN, A. W. 2017. Translational Genetic Modelling of 3D Craniofacial Dysmorphology: Elaborating the Facial Phenotype of Neurodevelopmental Disorders Through the "Prism" of Schizophrenia. *Curr Behav Neurosci Rep,* 4**,** 322-330.

WU, C., XIE, T., GUO, Y., WANG, D., QIU, M., HAN, R., QING, G., LIANG, K. & LIU, H. 2023. CDK13 phosphorylates the translation machinery and promotes tumorigenic protein synthesis. *Oncogene,* 42**,** 1321-1330.

YAO, T. P., OH, S. P., FUCHS, M., ZHOU, N. D., CH'NG, L. E., NEWSOME, D., BRONSON, R. T., LI, E., LIVINGSTON, D. M. & ECKNER, R. 1998. Gene dosage-dependent embryonic development and proliferation defects in mice lacking the transcriptional integrator p300. *Cell,* 93**,** 361-72.

YIGIT, G., BROWN, K. E., KAYSERILI, H., POHL, E., CALIEBE, A., ZAHNLEITER, D., ROSSER, E., BÖGERSHAUSEN, N., UYGUNER, Z. O., ALTUNOGLU, U., NÜRNBERG, G., NÜRNBERG, P., RAUCH, A., LI, Y., THIEL, C. T. & WOLLNIK, B. 2015. Mutations in CDK5RAP2 cause Seckel syndrome. *Mol Genet Genomic Med,* 3**,** 467-80.

YINGLING, J., TOYO-OKA, K. & WYNSHAW-BORIS, A. 2003. Miller-Dieker syndrome: analysis of a human contiguous gene syndrome in the mouse. *Am J Hum Genet,* 73**,** 475-88.

Figures

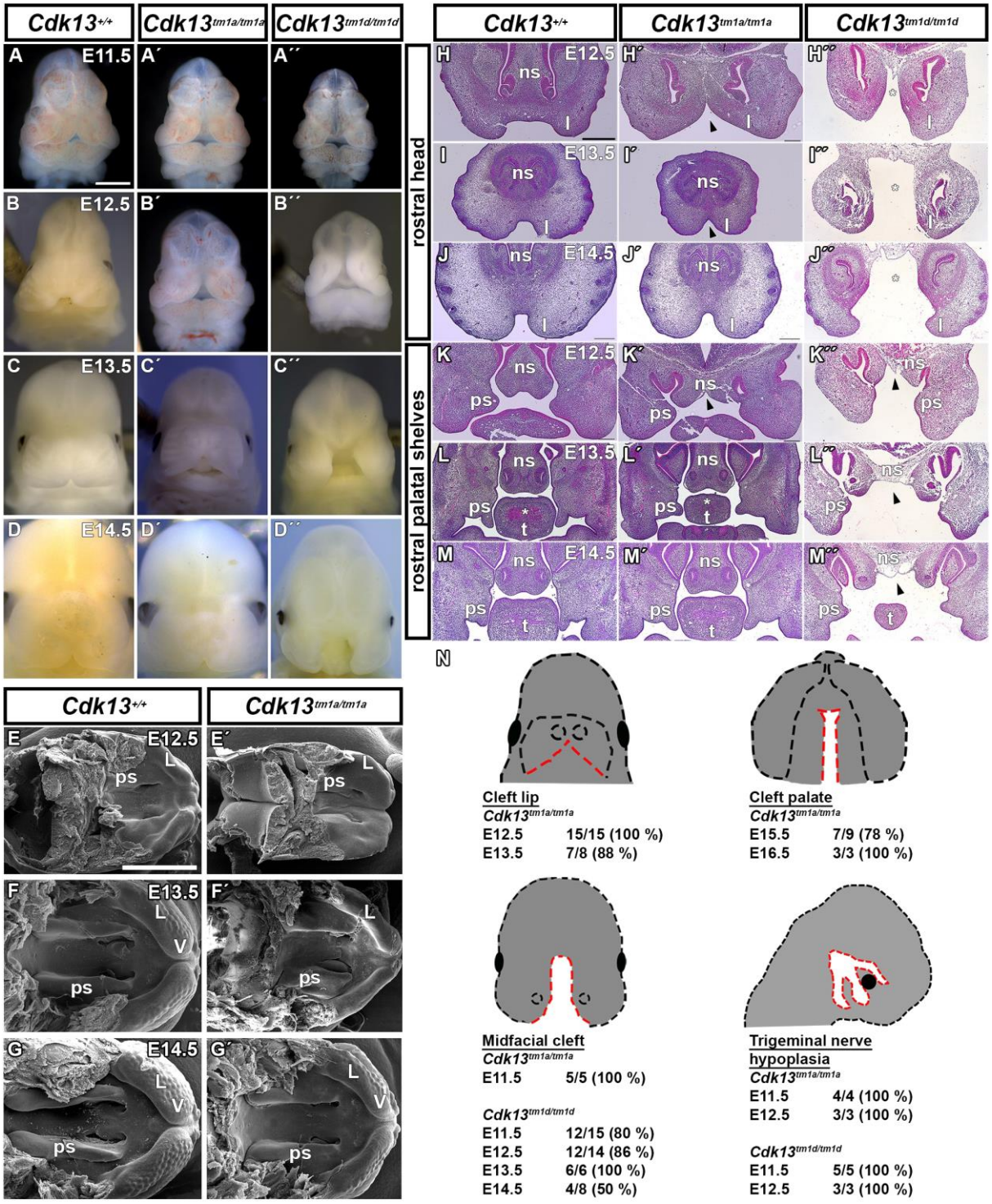

Fig. 1. *Cdk13*-deficient embryos display severe craniofacial clefting.

(A – D´´) Comparison of external craniofacial phenotype of the E11.5 - E14.5 embryos between individual genotypes (WT, *Cdk13*$^{tm1a/tm1a}$, *Cdk13*$^{tm1d/tm1d}$). **(E - G´)** Palatal view of the

E12.5 – E14.5 embryos using scanning electron microscope displaying differences in morphology of the palatal shelves, forming lips and vibrissae in hypomorphic (*Cdk13*$^{tm1a/tm1a}$) embryos compared to WT. **(H – M´´)** Hematoxylin-Eosin staining of the E12.5 – E14.5 frontal head sections. **(H – J´´)** Arrowheads point to the cleft lip in *Cdk13*$^{tm1a/tm1a}$ embryos and asterisks highlight the midfacial cleft in KO (*Cdk13*$^{tm1d/tm1d}$) embryos. **(K – M´´)** Arrowheads point to cleft nasal septum in both hypomorph and KO embryos. The palatal shelves development in the rostral region is altered in both genotypes compared to WT embryos. Hypoplastic muscles in the tongue are marked by asterisks. **(N)** Table displays frequency of severe craniofacial phenotypes (cleft lip, cleft palate, midfacial cleft, hypoplasia of the trigeminal nerve) within individual genotypes and embryonic developmental stages. Red dashed lines contour defective structures. L – lip; ns – nasal septum; ps – palatal shelf; t – tongue; V - vibrissae. Scale bars: macroscopic pictures - 1 mm, Hematoxylin-Eosin stained sections – 500 µm, SEM pictures – 1 mm.

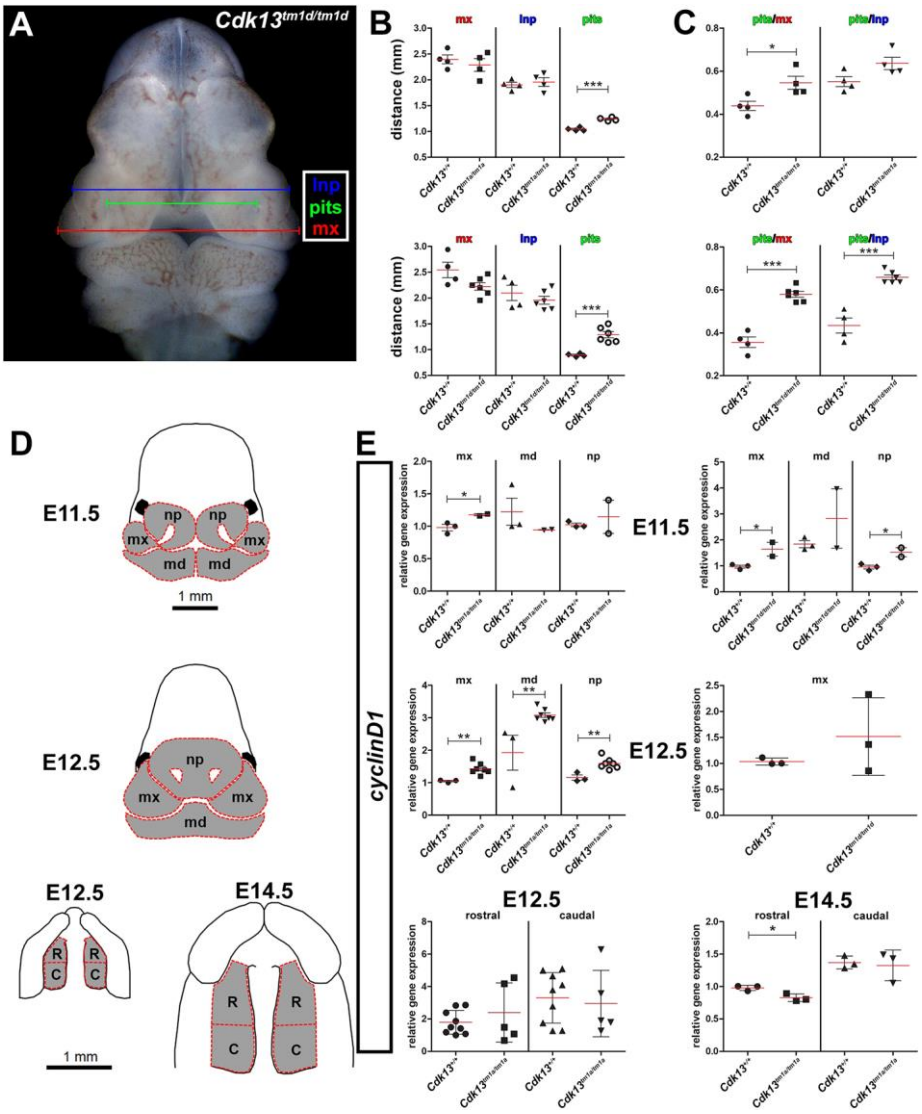

Fig. 2. Changes in facial morphometrics and cell proliferation in *Cdk13* mutant embryos.

(**A)** Schema of the measurements performed on the E11.5 embryonic heads (*Cdk13*$^{tm1d/tm1d}$ used as a representative). Distances between edges of the lateral nasal prominences (blue), edges of the maxillary prominences (red) and nasal pits (green) were measured. **(B)** Individual graphs displaying distances (mm) measured in E11.5 WT, hypomorphic and knockout embryos and **(C)** ratios calculated from the distances. **(D)** Schematic description of how individual tissues were dissected for quantification of the *CyclinD1* gene expression in E11.5/E12.5 mx, md and np, and R and C palatal shelves. (**E)** Quantification of changes in proliferation detected by *CyclinD1* gene expression by qPCR in the mx, md and np facial parts of the E11.5 and E12.5 and in rostral and caudal palatal shelves of the E12.5 and E14.5

hypomorph embryos. t - test; **0.001 < p < 0.01; *p < 0.05. C - caudal palate; lnp - lateral nasal prominence; md - mandibular prominence; mx - maxillary prominence; np - nasal prominence; pits - nasal pits; R - rostral palate.

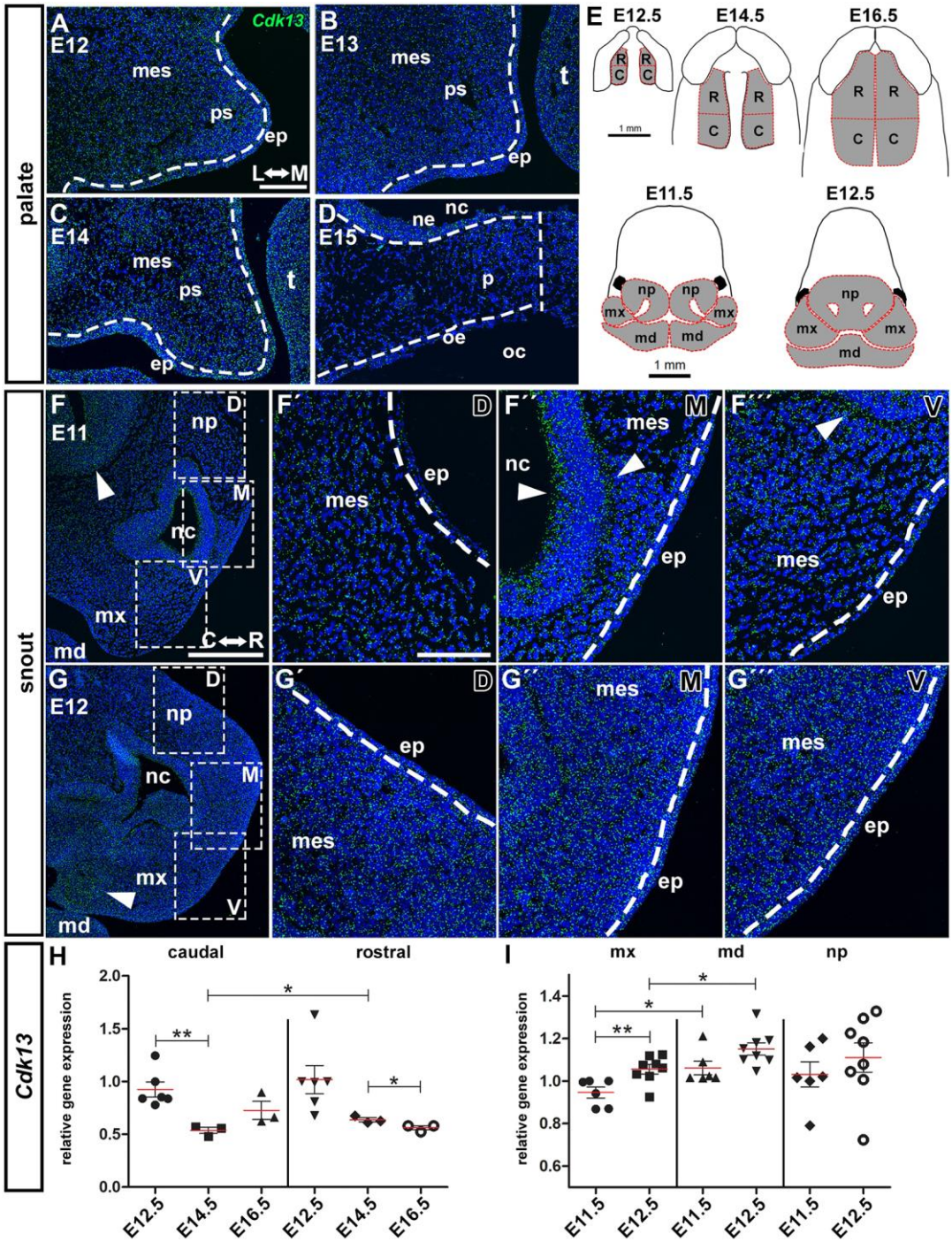

Fig. 3. Physiological gene expression of the *Cdk13* in the developing palatal tissues and snout detected by RNAScope and its quantification by qPCR.

(A–D) *Cdk13* (green) gene expression in the developing WT palatal shelves from E12 to E14 stages and in the fused secondary palate at E15 on transversal sections. White dashed lines separate mesenchyme from epithelium. Vertical white dashed line **(D)** highlights the secondary palate midline at E15. **(E)** Schematic description of how individual tissues were

dissected for quantification of the *Cdk13* gene expression. Expression was quantified in tissues dissected from rostral (R) and caudal (C) palatal shelves or palate at E12.5, E14.5 and E16.5 and in tissues dissected from mx, md and np at E11.5 and E12.5 **(F, G)** Lower power magnification of the *Cdk13* gene expression in the developing snout at E11 and E12 stages of WT embryos. White dashed line rectangles highlight regions used for higher power pictures in dorsal **(**D; **F´, G´)**, middle **(**M; **F´´, G´´)**, and ventral **(**V; **F´´´, G´´´)** areas. Arrowheads point to dense signal in the developing forebrain **(F)**, nasal epithelium **(F´´, F´´´)** at E11 and in the developing mx **(G)** at E12. White dashed lines separate mesenchyme and epithelium. Nuclei are counterstained with DAPI. **(H)** Quantification of the *Cdk13* gene expression by qPCR in the E12.5, E14.5 and E16.5 palatal shelves. **(I)** Quantification of the *Cdk13* gene expression by qPCR in the E11.5 and E12.5 mx, md and np. Unpaired two-tailed Student t - test; **0.001 < p < 0.01; *p < 0.05. C – caudal; ep – epithelium; np – nasal prominence; L – lateral; M – medial; mes – mesenchyme; md – mandibular prominence; mx – maxillary prominence; nc – nasal cavity; ne – nasal epithelium; oc – oral cavity; oe – oral epithelium; ps – palatal shelf; p - palate; R – rostral; t – tongue. Scale bars: palate – 100 µm; snout: lower power – 200 µm, higher power – 100 µm.

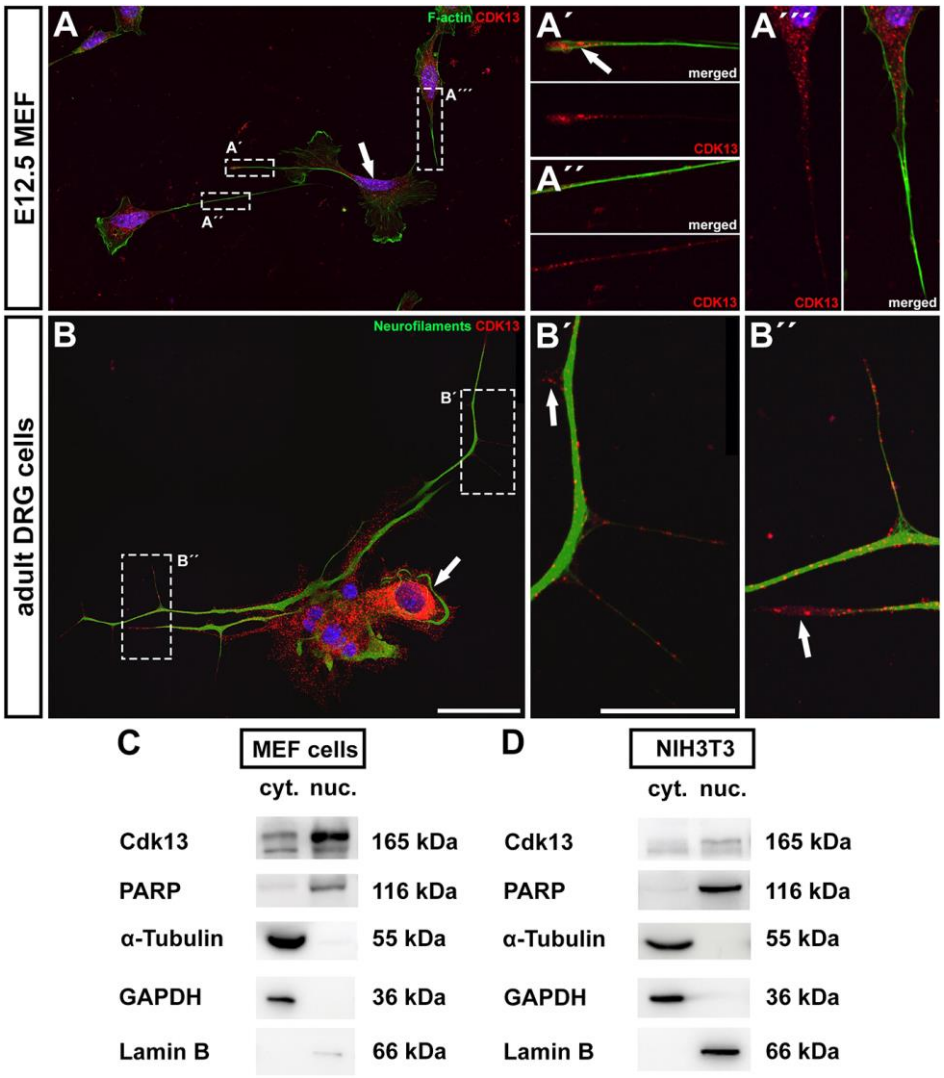

Fig. 4. CDK13 cellular localization via immunocytochemical and immunoblotting methods. **(A)** Lower power picture of CDK13 (red) and F-actin (green) expression in mouse embryonic fibroblasts (MEF) isolated from E12.5 embryonic bodies. Arrow points to the nuclear area with CDK13 expression. Dashed line rectangles highlight details of cellular outgrowths. **(A´-A´´´)** Details of CDK13 expression in the forming cellular processes. Arrow points to the apical area with enriched CDK13 expression **(A´)**. **(B)** Lower power picture of CDK13 (red) expression and neurofilaments (green, anti-2H3) in primary cells isolated from dorsal root ganglia of adult mice. Arrow points to the nuclear area with strong CDK13 expression. Dashed line rectangles highlight details on neurite outgrowths. **(B´, B´´)** Details of CDK13 expression in the forming neurite outgrowths. Arrows point to areas with CDK13 expression prior to neurofilament formation. Nuclei are counterstained with DAPI. Scale bars: (A-B´´) -

lower power – 50 µm, higher power – 20 µm **(C)** Immunoblots of CDK13 in cytoplasmic and nuclear extracts from primary MEF and NIH3T3 mouse fibroblasts **(D)**. The Lamin B and PARP1 were used as positive controls of nuclear fraction and α-Tubulin along with GAPDH were used as positive control of cytoplasmic fraction. Cyt.: cytoplasm; Nuc.: nucleus.

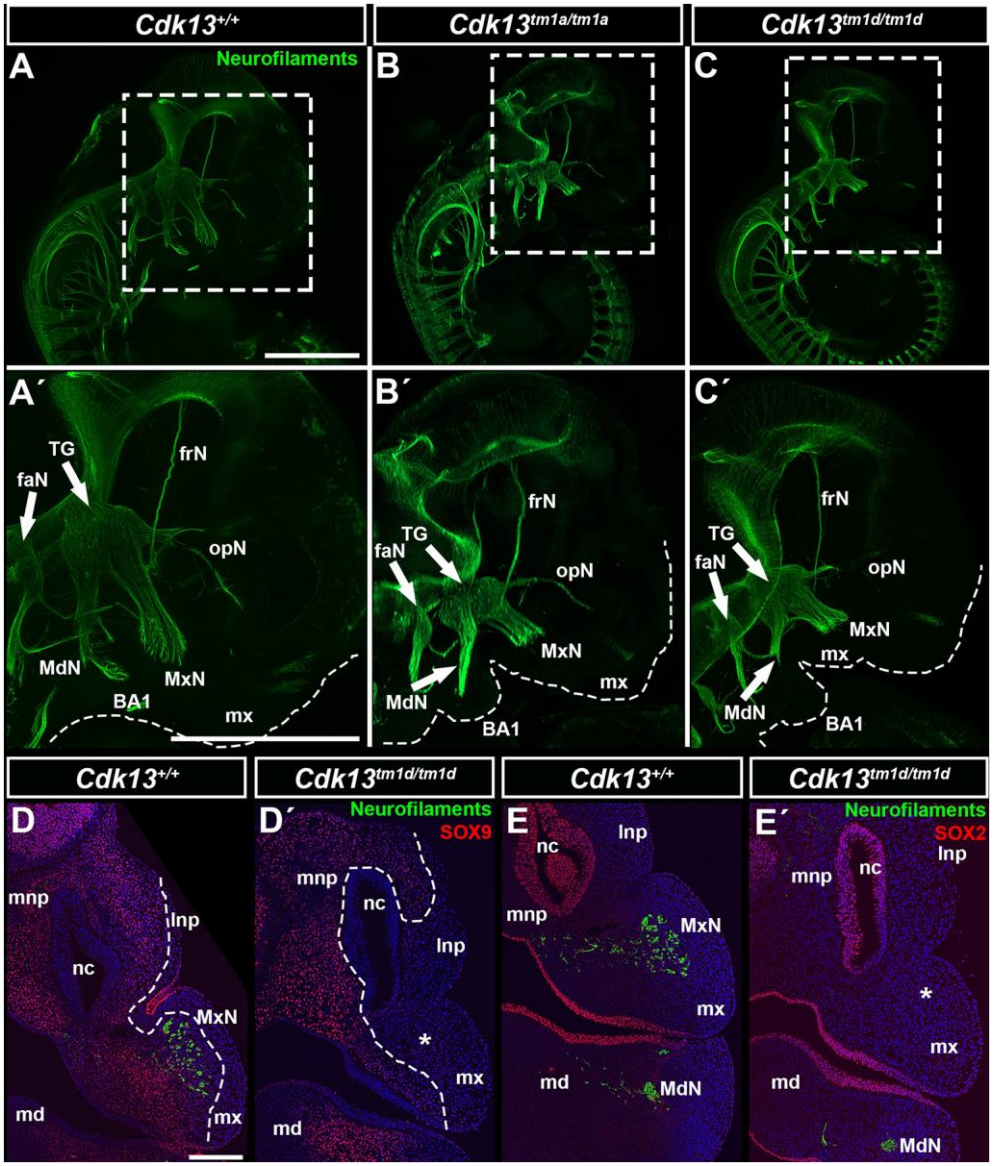

Fig. 5. Immunohistochemical detection of cranial nerves on whole mount embryos and histological sections.

(A-C) Development of neurons detected using anti neurofilaments antibody (green, anti-2H3) on the E11.5 WT, *Cdk13*$^{tm1a/tm1a}$ and *Cdk13*$^{tm1d/tm1d}$ embryos. Dashed line rectangles highlight detail of the craniofacial region. **(A´-C´)** Higher power pictures focused on cranial nerves in E11.5 embryos. Detail displays the basis of the facial nerve, and divisions of the trigeminal nerve – mandibular, maxillary and ophthalmic nerves, including the frontal branch nerve of the ophthalmic nerve. Dashed line highlights edges of the maxillary prominences and branchial arch 1. Note underdeveloped and hypoplastic all three divisions of the TG nerve in *Cdk13*$^{tm1a/tm1a}$ **(B´)** and especially in *Cdk13*$^{tm1d/tm1d}$ **(C´)** embryos. **(D-E´)** Immunohistochemical detection of neurofilaments (anti-2H3), SOX9 and SOX2 on frontal

sections of E11.5 embryos. Missing maxillary nerves in *Cdk13*-deficient embryos marked by asterisks **(D´,E´)**. White dashed lines label areas of the SOX9 expression **(D,D´)**. Scale bars: whole mount - 1 mm; IHC sections – 20 µm. BA1 – 1. branchial arch; faN – frontal and acoustic nerves; frN – frontal branch of the ophthalmic nerve; MdN – mandibular branch of the trigeminal nerve; mx – maxillary prominence; MxN – maxillary branch of the trigeminal nerve; opN – ophthalmic branch of the trigeminal nerve; TG – trigeminal ganglion.

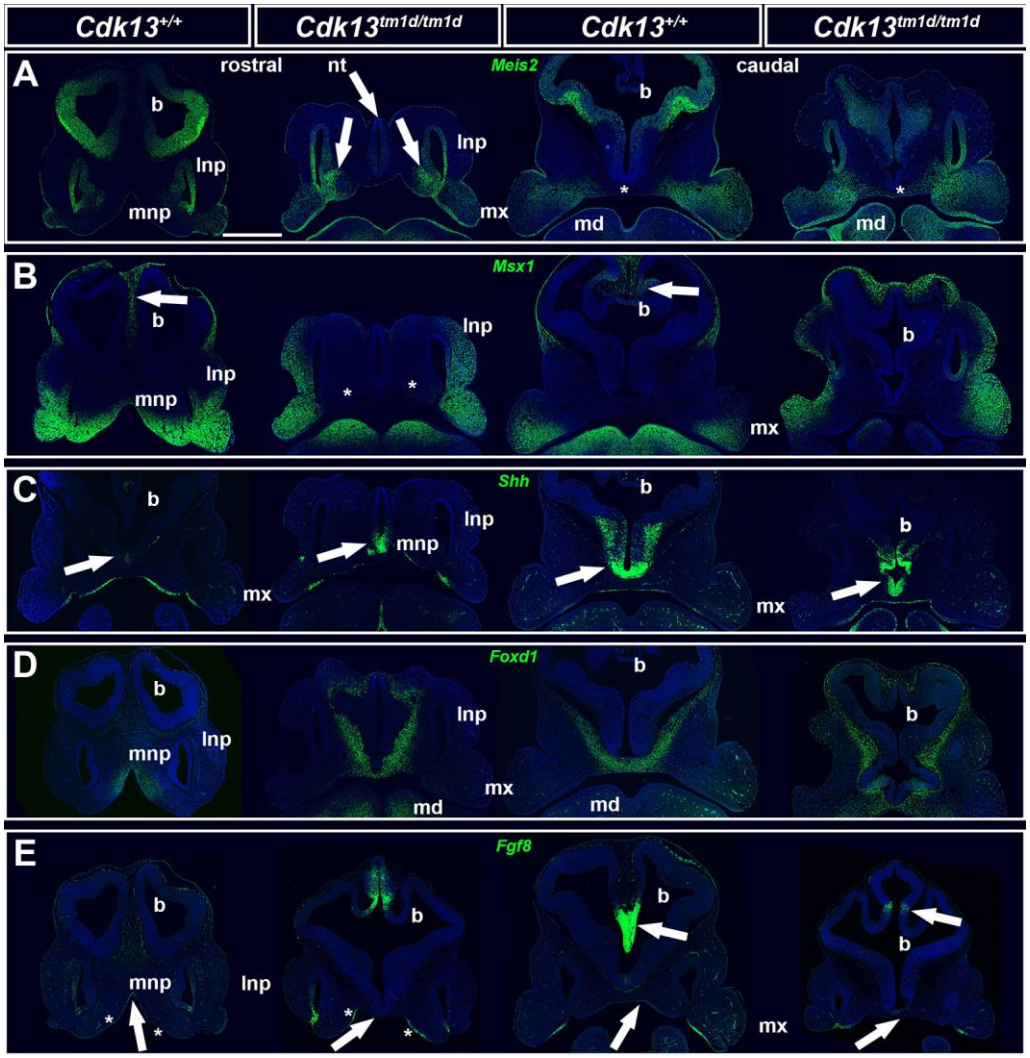

Fig. 6. RNAScope detection of the *Meis2*, *Msx1*, *Shh*, *Foxd1* and *Fgf8* gene expression on the frontal sections of E11.5 embryos.

(A-E) Gene expression was detected in the maxillary, mandibular, lateral and medial nasal prominences and in the developing brain of the *Cdk13*-knockout embryos. All the individual gene patterns for *Meis2* **(A)**, *Msx1* **(B)**, *Shh* **(C)**, *Foxd1* **(D)** and *Fgf8* **(E)** are displayed as a green signal. Pictures are separated into 4 columns presenting rostral (two left panels) and caudal sections (two right panels). Scale bar: 500 µm. b - brain; lnp – lateral nasal prominence; md – mandibular prominence; mnp – medial nasal prominence; mx – maxillary prominence; nt – neural tube.

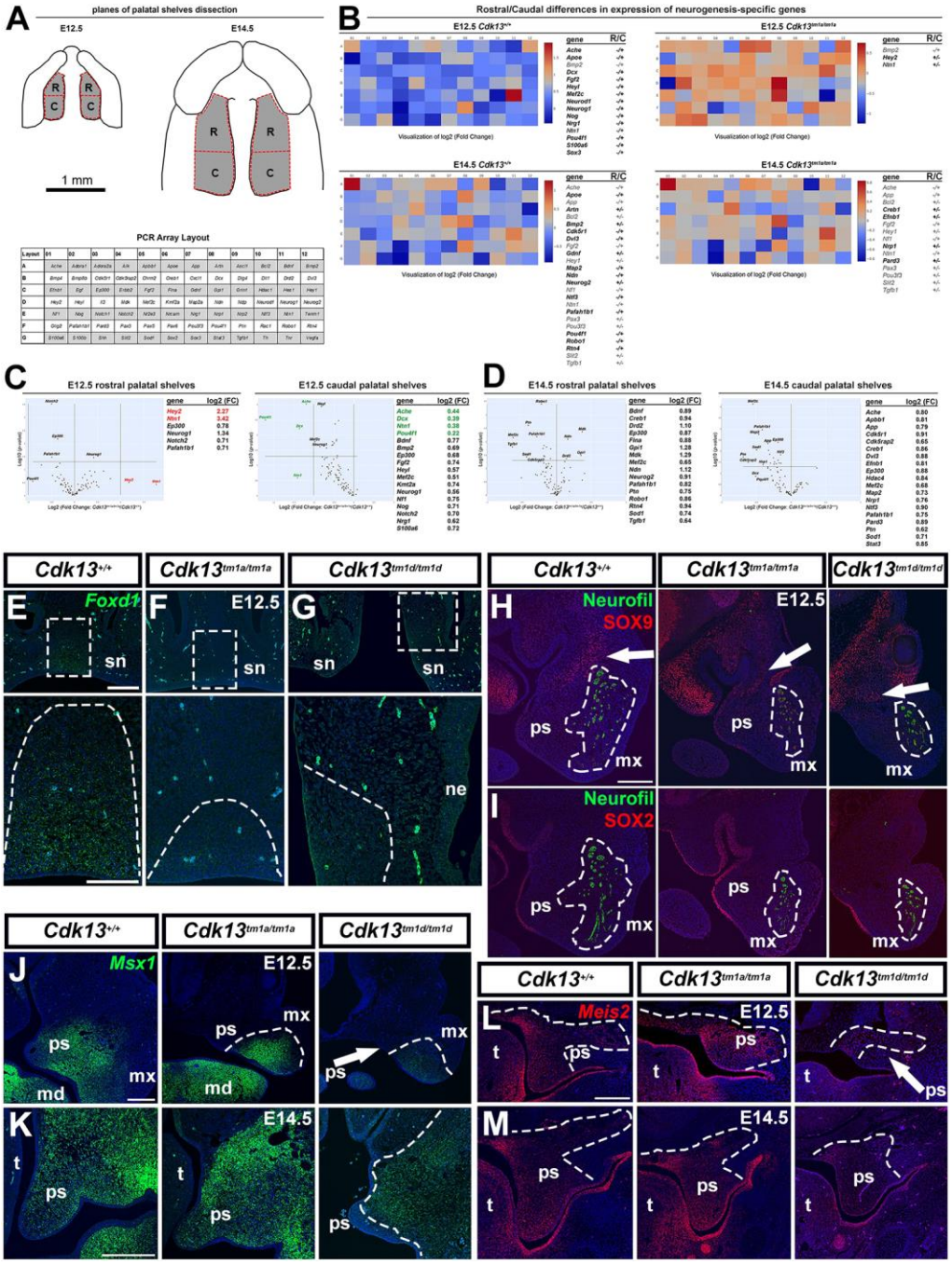

Fig. 7. Gene expression quantification analysis of the neurogenesis-associated molecules in the *Cdk13*$^{tm1a/tm1a}$ palatal shelves and *in situ* gene and protein expression on sections.

(A-D) PCR Array for mouse neurogenesis specific genes performed separately on tissues dissected from the E12.5 and E14.5 rostral and caudal palatal shelves of *Cdk13*$^{tm1a/tm1a}$ embryos. **(A)** Schema of dissected regions (R – rostral; C – caudal) from the E12.5 and E14.5 palatal shelves and table displaying layout of individual genes detected in PCR Array. **(B)** Heat maps and tables presenting rostral/caudal differences in expression of

neurogenesis-specific genes separately in control (WT) embryos (upper and lower left) and in *Cdk13*$^{tm1a/tm1a}$ embryos (upper and lower right). In tables, genes marked with black text color are enriched either in the R or C palatal shelves. Genes marked with grey text color are expressed in the palatal regions in similar extent. Note the changed ratio of the gene expression polarity between WT and *Cdk13*-deficient palatal shelves (differences between genes expressed either in the R or C palatal shelves are much lower in *Cdk13*-deficient tissues). **(C)** Volcano plots and tables with log2 Fold Changes displaying significantly deregulated expression of neurogenesis-specific genes individually in the E12.5 and **(D)** E14.5 *Cdk13*-deficient palatal shelves. In tables, genes marked with red text color are strongly upregulated and genes marked with green text color are strongly downregulated in *Cdk13*-deficient embryos compared to control embryos. The p values are calculated based on a Student's t-test of the replicate 2^(- Delta C_T) values for each gene in the control group and test groups. The p-value calculation used is based on parametric, unpaired, two-sample equal variance, two-tailed distribution.

(E-G) RNAScope detection of *Foxd1* (green) *in situ* gene expression on sections of E12.5 embryos from the rostral snout region. White dashed line rectangles highlight regions for detailed pictures. Dashed lines in detailed pictures outline *Foxd1* expression domains **(H-I)** Immunohistochemical detection of neurofilaments (green, anti-2H3), SOX9 (red) and SOX2 (red) expression on sections of E12.5 embryos. White arrows point to regions enriched with SOX9-positive cells. White dashed lines outline regions with 2H3 signal representing developing maxillary nerves. **(J-K)** RNAScope detection of *Msx1* (green) *in situ* gene expression on sections of E12.5 and E14.5 embryos from the rostral palate region. White dashed lines outline *Msx1*-positive regions. **(L-M)** RNAScope detection of *Meis2* (red) *in situ* gene expression on sections of E12.5 and E14.5 embryos from the caudal palate region. White dashed lines outline *Meis2*-positive regions. Scale bars: 200 µm; *Foxd1* detail – 100 µm. md – mandibular prominence; mx – maxillary prominence; ne – nasal epithelium; ps – palatal shelves; sn – snout; t – tongue.

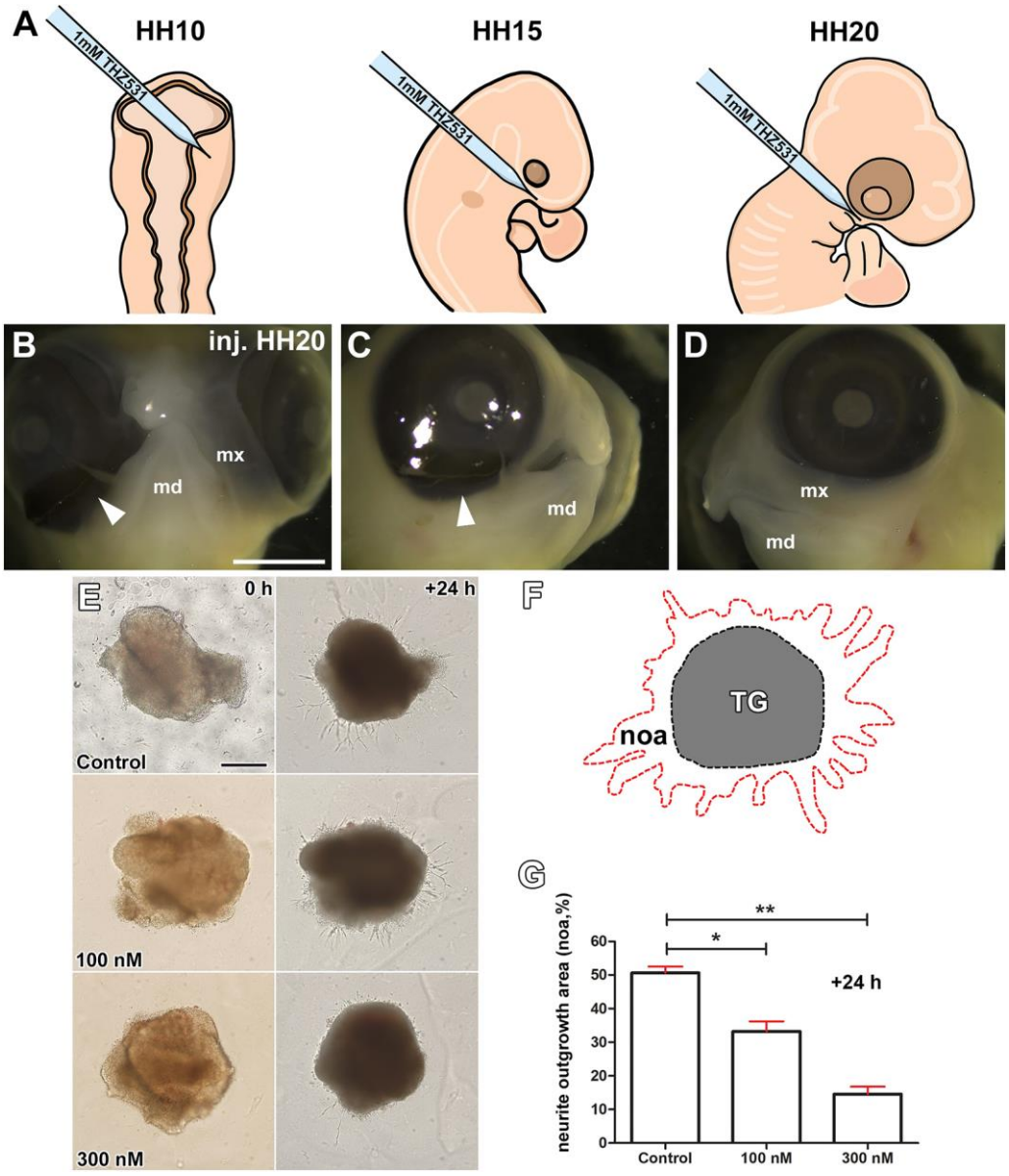

Fig. 8. Chemical inhibition of the CDK12 and CDK13 leads to embryonic facial malformations and altered neurite outgrowth.

(A) Schematic drawing showing injection side of the THZ531 inhibitor to the maxillary prominences in the HH10, HH15, and HH20 chicken followed by 4-6 days of incubation. **(B-D)** Macroscopic pictures focused on ventral and lateral regions of the embryonic head. **(B)** Missing maxillary prominence visible on both ventral and **(C)** lateral regions (right side was injected) highlighted by white arrowheads. **(D)** Left control untreated (not injected) side with no defect. Scale bar: 3 mm. md – mandibular prominence; mx – maxillary prominence. **(E)** General morphology of *ex vivo* trigeminal ganglia explants in three groups (Control, 100 nM, 300 nM) captured at the beginning of cultivation (0 h) and at the end (24 h). Note different

length and number of neurite outgrowths under different conditions. Scale bar: 200 µm. **(F)** Scheme shows areas used to measure differences in outgrowth of neurites (red dashed line) from trigeminal ganglia (TG, grey area encircled with black dashed line). Neurite outgrowth area is marked as noa. **(G)** Graphical representation of neurite outgrowth areas (noa) after 24 hours of cultivation with different concentrations (Control, 100 nM, 300 nM) of the THZ531 inhibitor. Unpaired two-tailed Student t - test; **0.001 < p < 0.01; *p < 0.05.

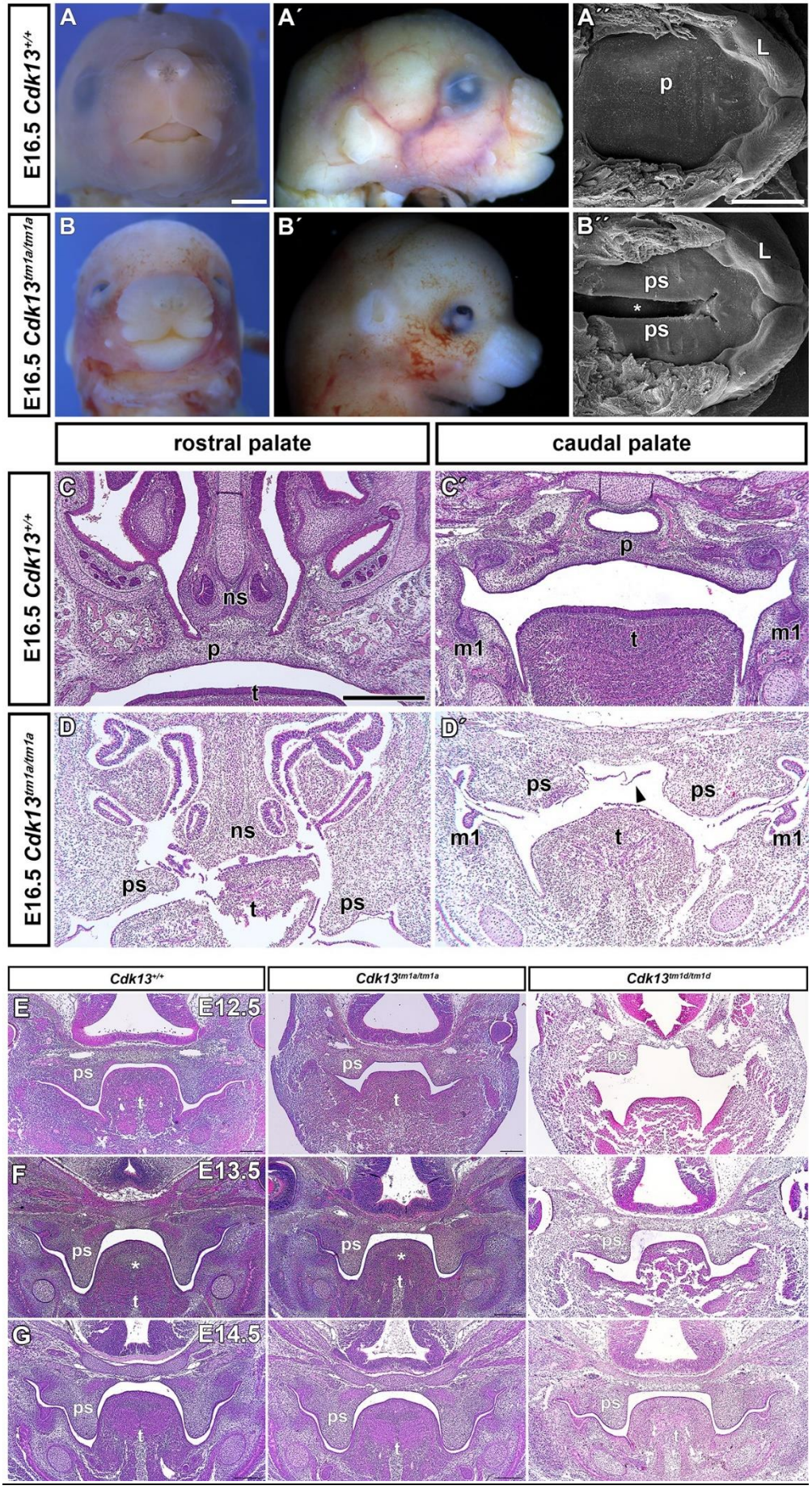

Fig. S1. Craniofacial phenotype of *Cdk13*-deficient embryos.

(A-B´) External craniofacial phenotype of WT and *Cdk13*$^{tm1a/tm1a}$ embryos at E16.5 developmental stage in frontal and side views. Mutant embryos rather resemble earlier developmental stage. (**A´´, B´´)** Palatal view of the WT and mutant embryos using scanning electron microscope displaying the morphology of the palatal shelves, forming lips and vibrissae. Star marks visible cleft palate between palatal shelves in mutant embryo. (**C–D´)** Transversal Hematoxylin-Eosin-stained sections of the rostral and caudal palate in WT and mutant embryos at E16.5. Rostral area in *Cdk13*$^{tm1a/tm1a}$ embryo (**D**) is typical by the underdeveloped palatal shelves with intervening tongue between them resembling earlier developmental stage. In caudal palate (**D´´**, first molar level) of *Cdk13*$^{tm1a/tm1a}$ embryo, arrowhead points to visible cleft palate. L – lip, m1 – first molar, ns – nasal septum, p – palate, ps – palatal shelf, t – tongue. Scale bars: 1 mm.

(E-G) HE-stained transversal sections through the developing caudal palate at E12.5, E13.5 and E14.5 stages. Note underdeveloped palatal shelves (ps) in both mutant genotypes, close proximity of the neural tube with the oronasal cavity in E12.5 *Cdk13*$^{tm1d/tm1d}$ embryo and reduced tongue musculature in E13.5 mutant embryos (asterisk). ps – palatal shelf; t – tongue.

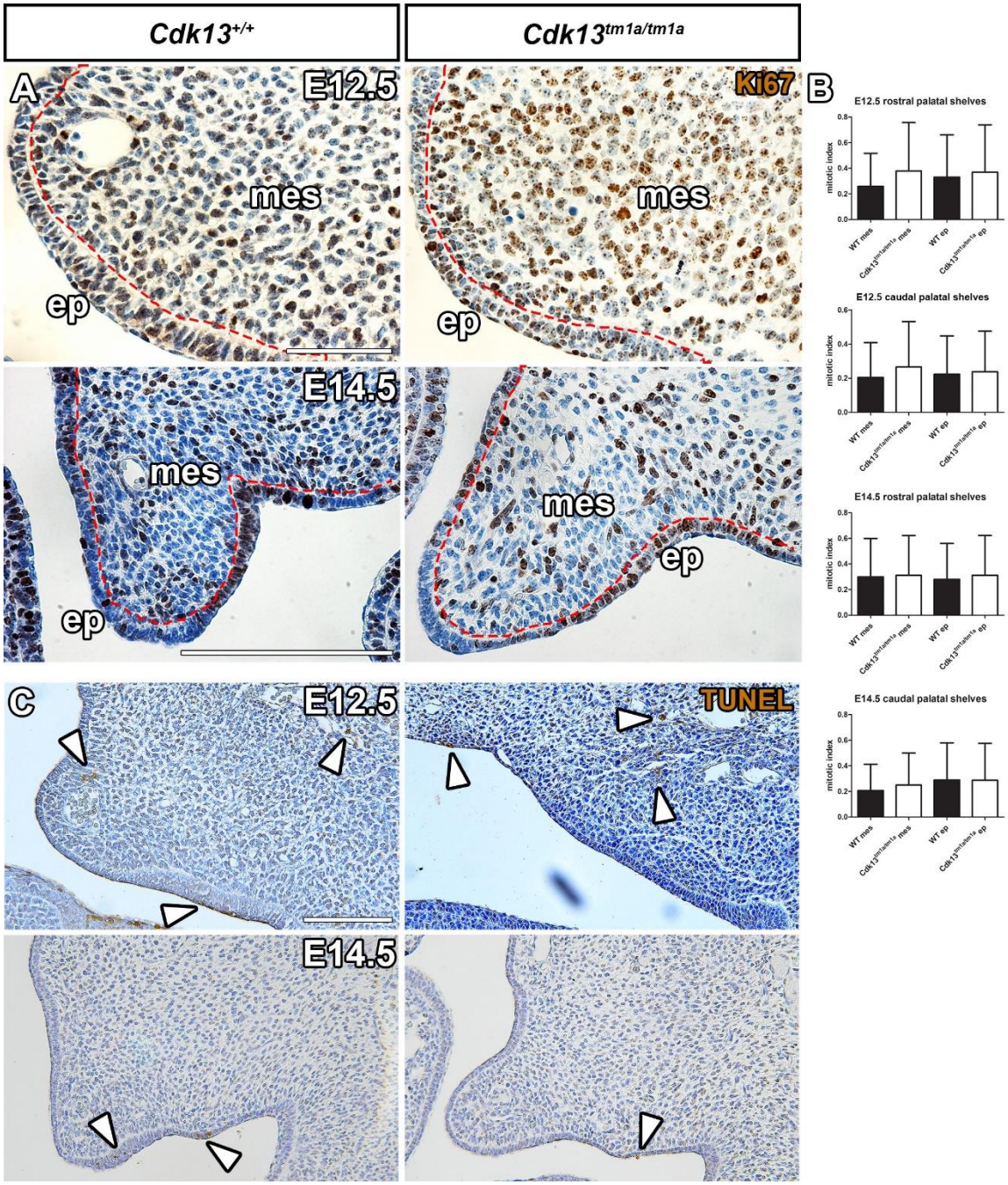

Fig. S2. Immunohistochemical detection of proliferating cells using Ki-67 antibody and detection of apoptotic cells by TUNEL Assay in the developing palatal shelves.

(A) Immunohistochemical detection of Ki-67-positive (brown) cells as a marker of proliferating cells in E12.5 and E14.5 palatal shelves on frontal sections. Palatal mesenchyme and epithelium are distinguished by a red dashed lines. Nuclei are counterstained with hematoxylin. Scale bars: 100 µm **(B)** Mitotic index counted from the Ki-67-positive cells detected by immunohistochemistry. Cells were counted independently in the rostral and caudal palatal shelves and separately in the palatal mesenchyme (mes) and epithelium (ep). Black columns represent WT embryos and white *Cdk13*$^{tm1a/tm1a}$ embryos. **(C)** Detection of the apoptotic cells by TUNEL assays on frontal sections of the E12.5 and E14.5 embryos. TUNEL-positivity is shown in brown, nuclei are counterstained by hematoxylin. Arrowheads point to positive signal. Scale bar: 500 µm. ep – epithelium; mes – mesenchyme.

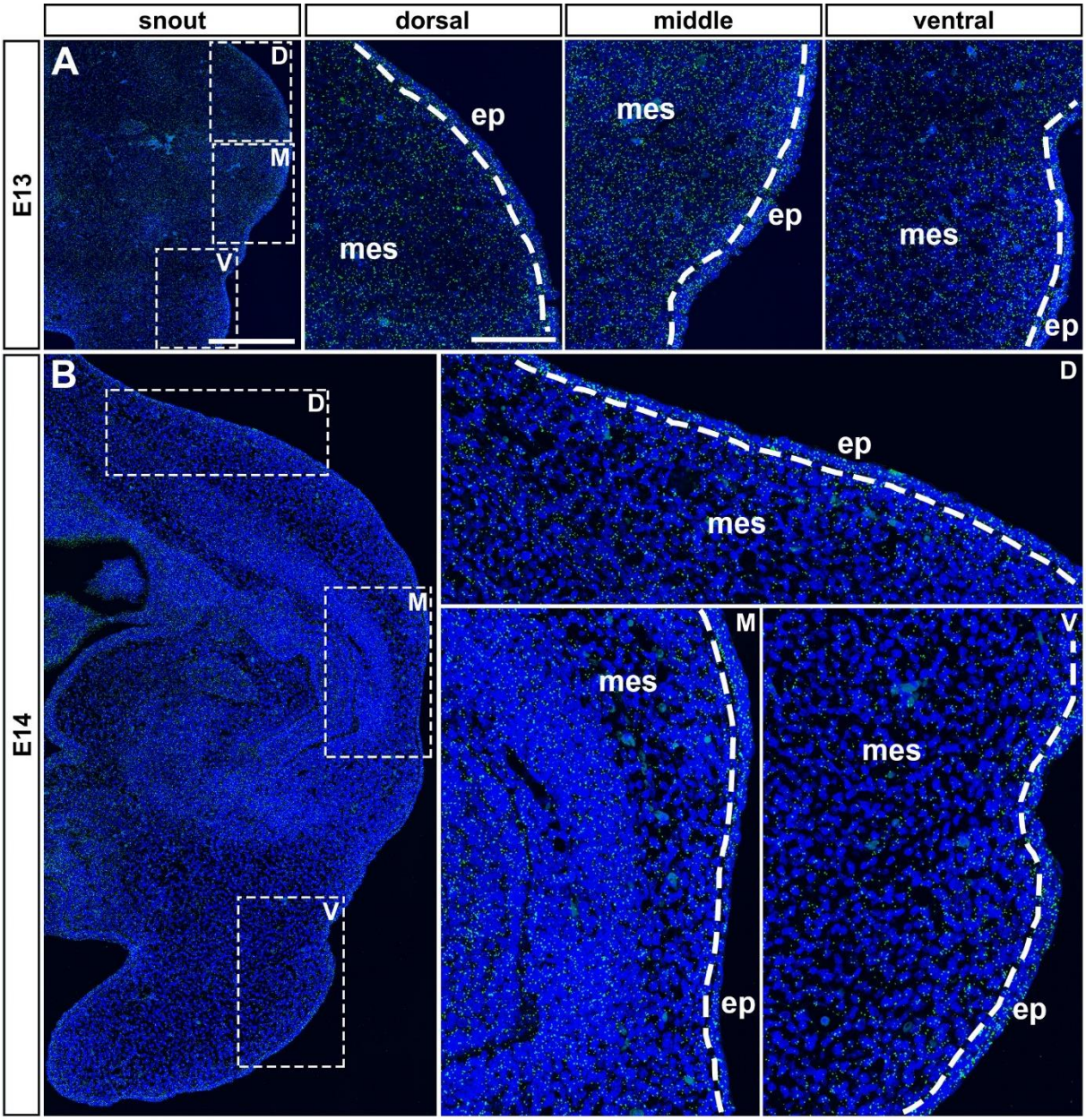

Fig. S3. Physiological expression of the *Cdk13* in the developing snout.

(A, B) RNAScope detection of the *Cdk13* (green) gene expression pattern in WT embryos. Lower power magnification of the *Cdk13* expression in the developing snout at E13 and E14 stages. White dashed line rectangles highlight regions used for higher power pictures in dorsal **(**D**)**, middle **(**M**)** and ventral **(**V**)** areas. Scale bars: lower power – 300 µm; higher power - 100 µm. ep – epithelium; mes – mesenchyme.

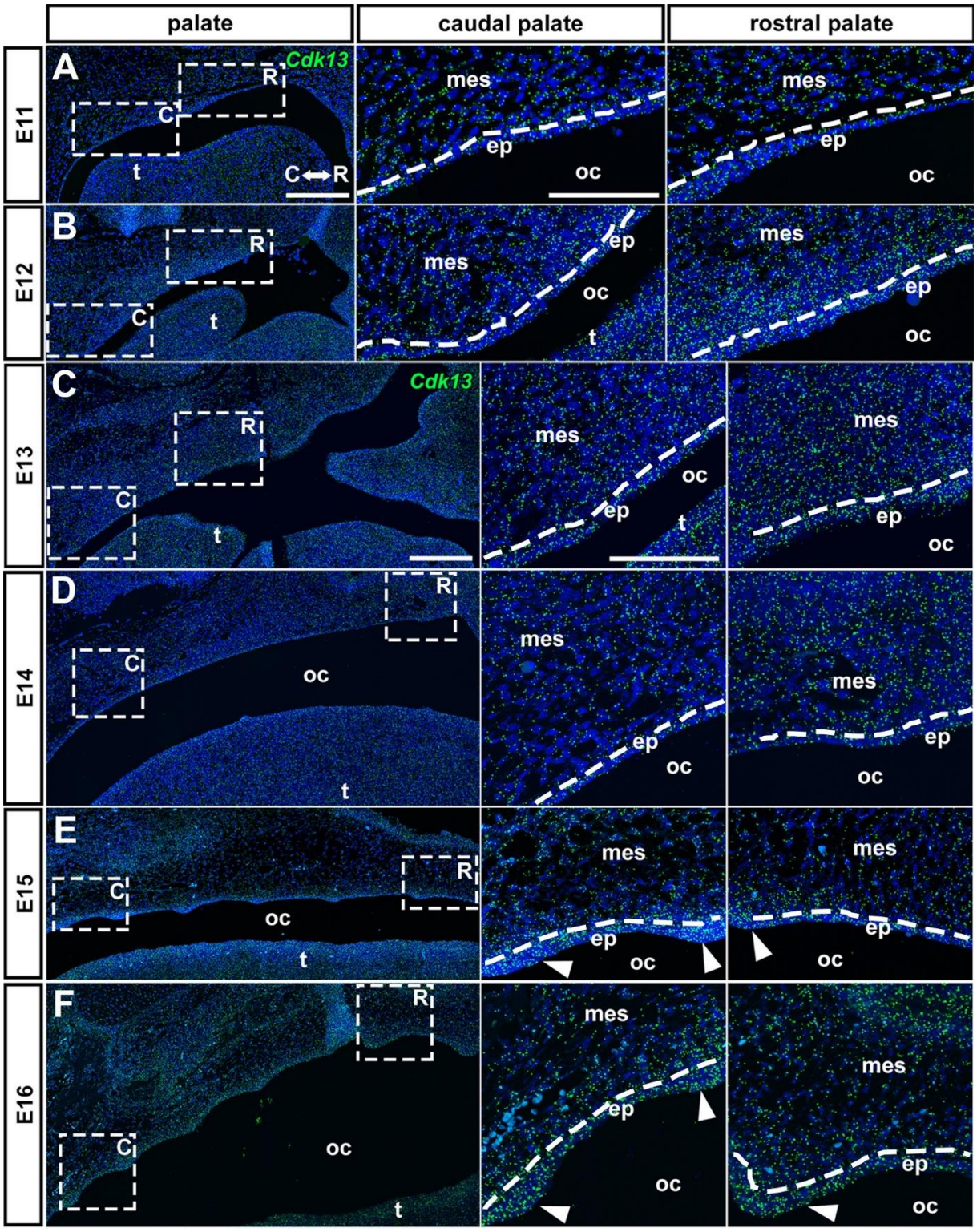

Fig. S4. Physiological expression of the *Cdk13* in the developing secondary palate.

(A–F) RNAScope detection of the*Cdk13* (green) in the WT palatal shelves from E12 to E16 stages sagittal sections. Lower power magnification of the *Cdk13* gene expression shows its distribution along rostral-caudal axis. White dashed line rectangles highlight regions used for higher power pictures in caudal **(**C**)** and rostral **(**R**)** regions. Arrowheads point to dense expression of the *Cdk13* in the palatal ridges in E15 and E16 embryos. Scale bars: lower power – 200 µm; higher power – 100 µm. ep – epithelium; mes – mesenchyme; oc – oral cavity; t – tongue.

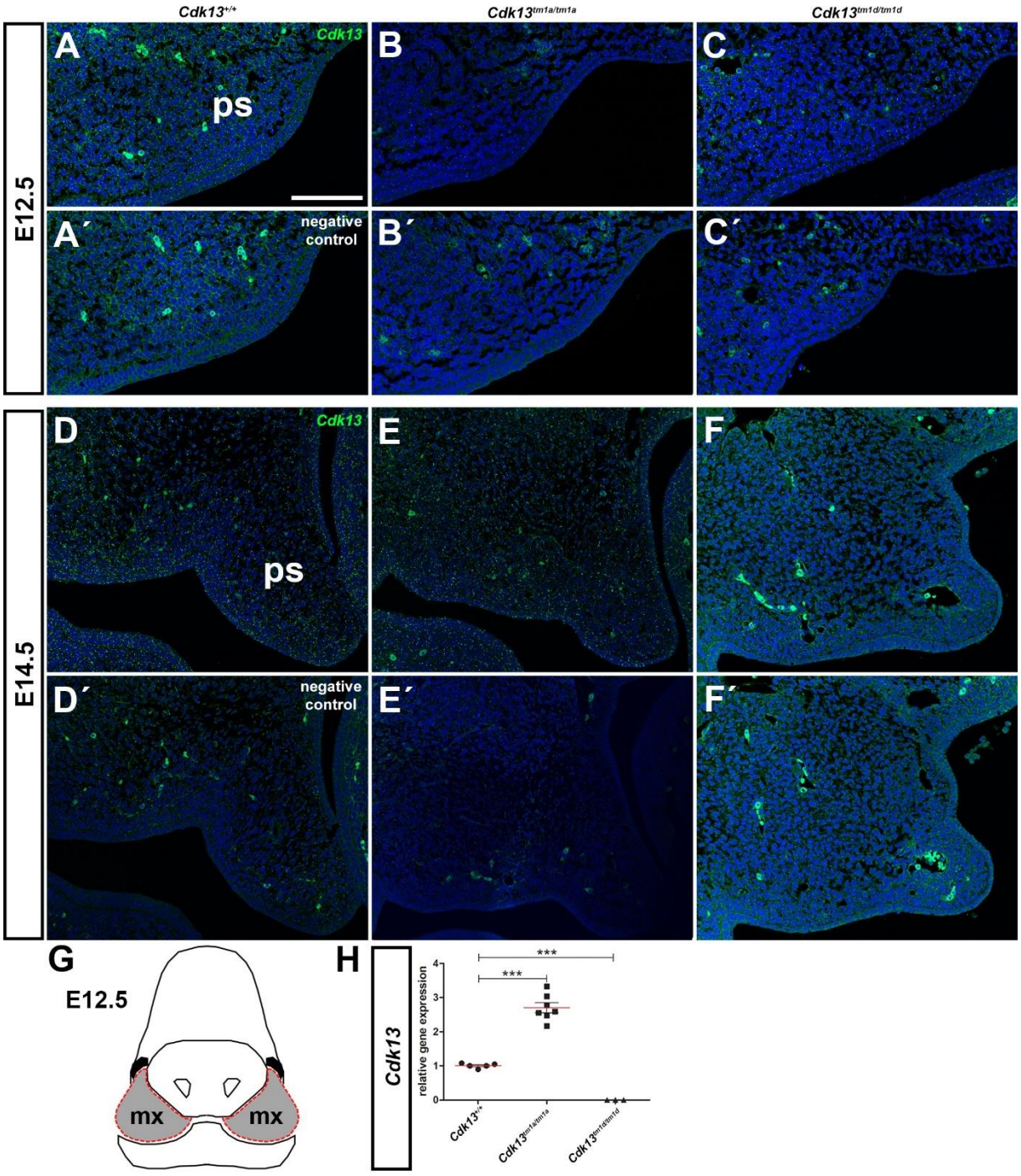

Fig. S5. *Cdk13* gene expression in the facial structures.

(A, A´) RNAScope detection showing pictures with the *Cdk13* (green) gene expression and negative control staining in the forming palatal shelf of E12.5 WT embryo, **(B, B´)** E12.5 *Cdk13*$^{tm1a/tm1a}$ and in **(C,C´)** E12.5 *Cdk13*$^{tm1d/tm1d}$ embryos. **(D,D´)** Pictures showing *Cdk13* (green) gene expression and negative control staining in the forming palatal shelf of E14.5 WT embryo, **(E, E´)** E14.5 *Cdk13*$^{tm1a/tm1a}$ and in **(F,F´)** E14.5 *Cdk13*$^{tm1d/tm1d}$ embryos. Note the specific RNAScope expression pattern shown as dots present in *Cdk13* stained sections and missing in negative control samples. Scale bar: 100 µm. **(G)** Schematic description what tissues and how were dissected for quantification of the *Cdk13* gene expression. **(H)** Quantification of the *Cdk13* expression using qPCR in E12.5 maxillary prominences of all the three genotypes. The used TaqMan probe spans exons 3 and 4 (exons missing in the *Cdk13*$^{tm1d/tm1d}$ animals). Unpaired two-tailed Student t - test; **0.001 < p < 0.01; *p < 0.05.

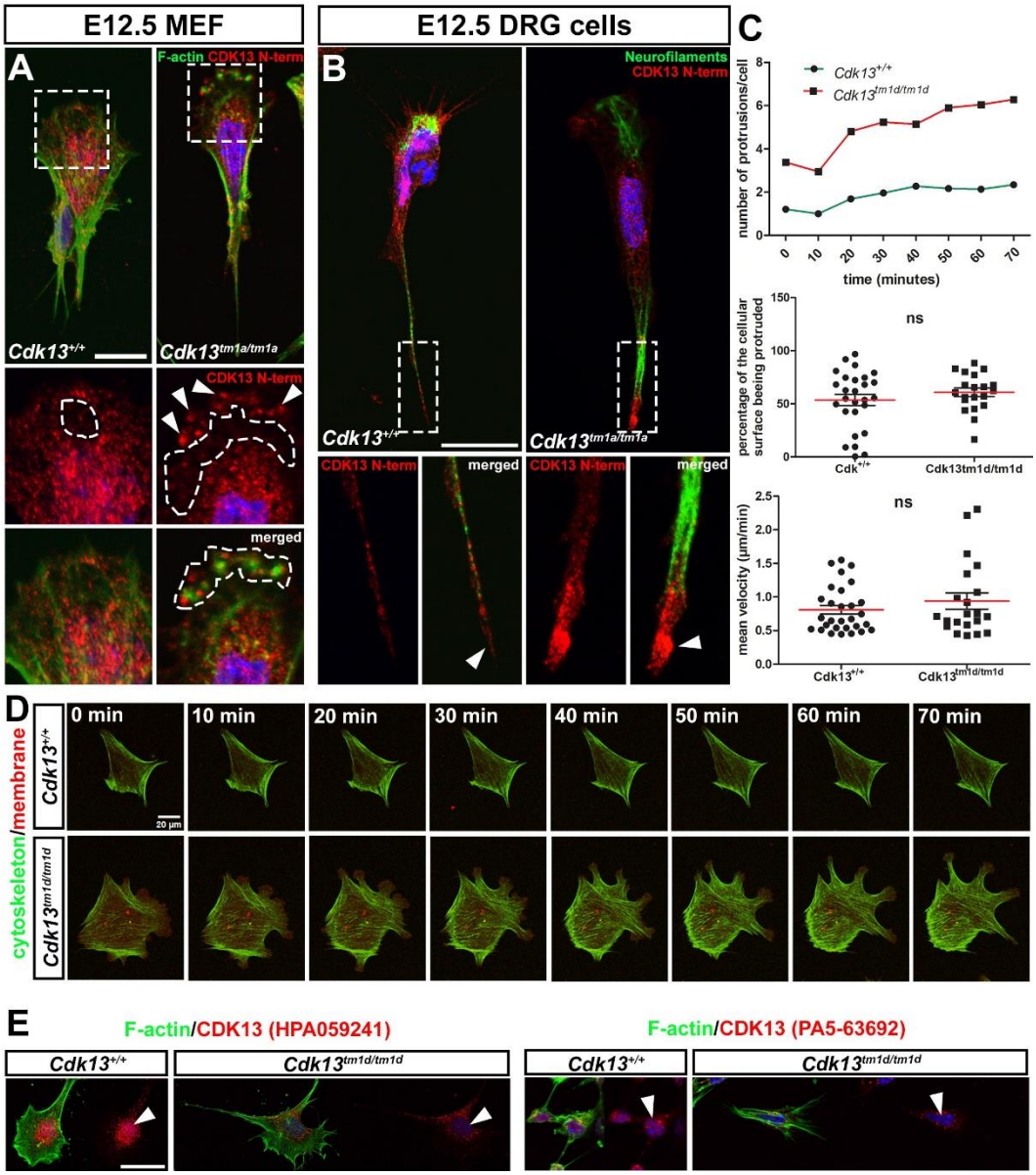

Fig. S6. Immunocytochemical localization of the CDK13 in control and *Cdk13*-deficient cells.

(A) Detection of the truncated form of CDK13 (red) in E12.5 *Cdk13*$^{tm1a/tm1a}$ MEF cells using anti N-terminal end CDK13 antibody. Dashed line rectangles highlight details on cellular outgrowths. Detailed pictures focus on aggregates of the truncated CDK13 in the cellular protrusions (arrowheads), CDK13-negative area (dashed line region, red) and colocalization of the truncated CDK13 with F-actin (green) deposits (dashed line region, merged). **(B)** Detection of the truncated form of CDK13 (red) in E12.5 *Cdk13*$^{tm1a/tm1a}$ DRG cells using anti N-terminal end CDK13 antibody colocalized with neurofilaments (green, anti-2H3). Dashed line rectangles highlight details on long cellular outgrowths. Detailed pictures focus on accumulation of the truncated CDK13 in distal part of the cellular outgrowth (arrowhead, merged). **(C)** Graphical representation of cells being tracked using Live Cell Imaging. Upper graph displays several protrusions per cell produced during time. Middle dot plot demonstrates percentage of the cellular surface protruded from cells. Lower dot plot displays comparison of the control and KO cells in the ability to move (mean velocity, micrometers per minute). **(D)** Changes of the morphology of control and KO cells in time using Live Cell Imaging. Green color represents cytoskeleton, red color highlights membrane. These cells were picked as cells with representative phenotype specific for each genotype. **(E)** Left panel shows protein expression of the CDK13 in control and KO cells using HPA059241 antibody. Right panel displays protein expression of the CDK13 in control and KO cells using PA5- 63692 antibody. Nuclei were counterstained with DAPI. Arrowheads point to signal detected using anti-CDK13 antibodies (red) in nuclei. Scale bars: (A) – 10 µm; (B) – 20 µm; (D,E) – 20 µm.

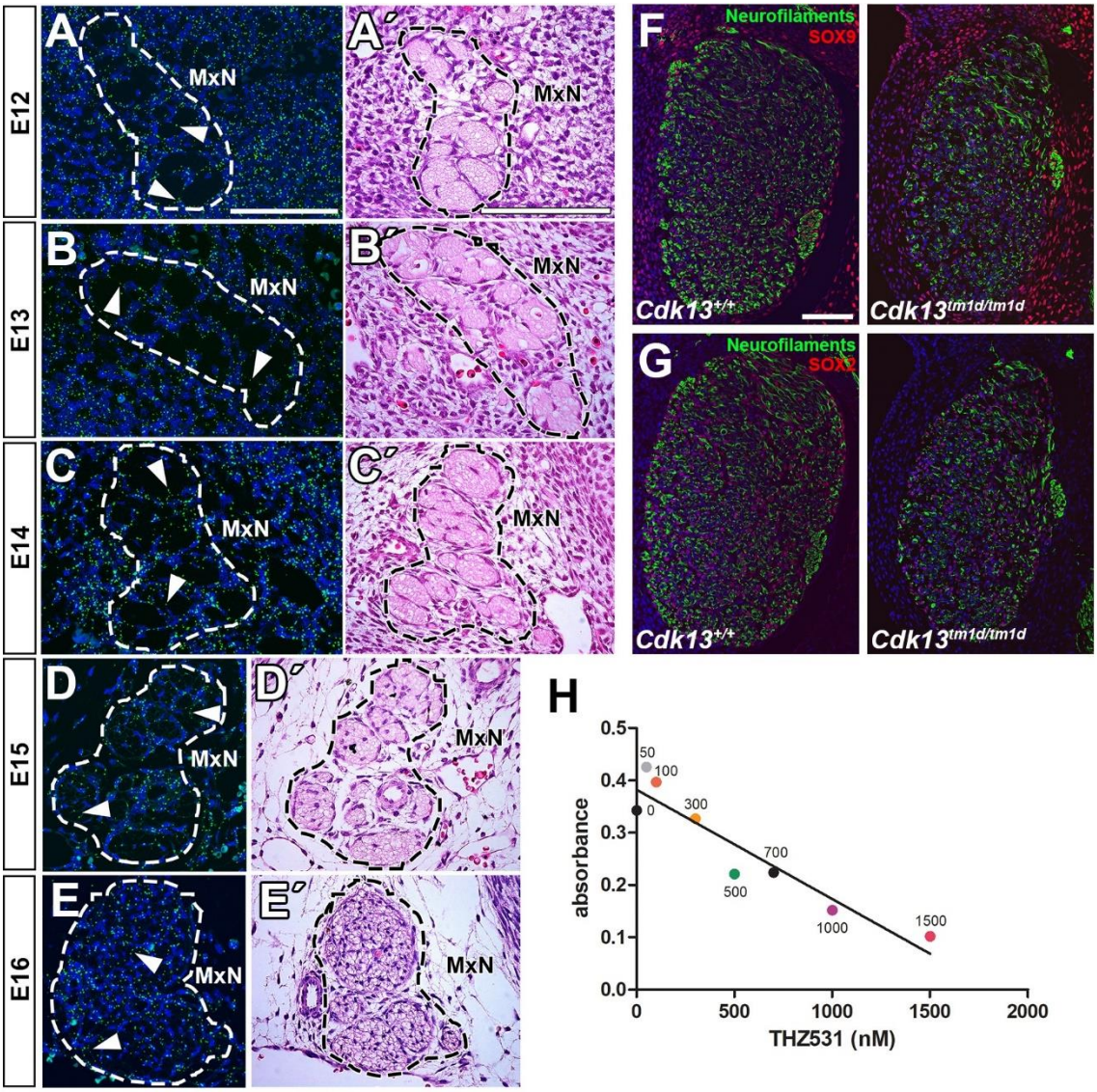

Fig. S7. *Cdk13* expression and the effect of its downregulation on development of trigeminal ganglion.

RNAScope detection of the *Cdk13* in maxillary nerve.

(**A-E)** RNAScope detection of the *Cdk13* expression in the forming maxillary nerve. Arrowheads point to *Cdk13* localization in the cellular outgrowths protruding to the developmental nerves. Dashed line areas outline nerves. Nuclei are counterstained with DAPI. **(A´-E´)** HE-stained alternative sections display formation of the maxillary nerve. Scale bar: µm 100. MxN – maxillary nerve.

Immunohistochemical detection of neurofilaments and SOX-family proteins in trigeminal ganglion.

(F,G) Immunohistochemical detection of neurofilaments (green), SOX9 (red) and SOX2 (red) in the developing trigeminal ganglion in E11.5 embryos on transversal sections. Note reduced size of the trigeminal ganglion in *Cdk13*$^{tm1d/tm1d}$ embryo. Nuclei are counterstained with DAPI. Scale bar: 100 µm.

THZ531 cytotoxicity tested by MTT Assay.

(H) A graph showing decreasing absorbance with the increasing cytotoxicity of the THZ531 inhibitor used on cells isolated from the trigeminal ganglions. 100 nM and 300 nM concentrations were than used to treat trigeminal ganglia in ex vivo cultivation experiments.

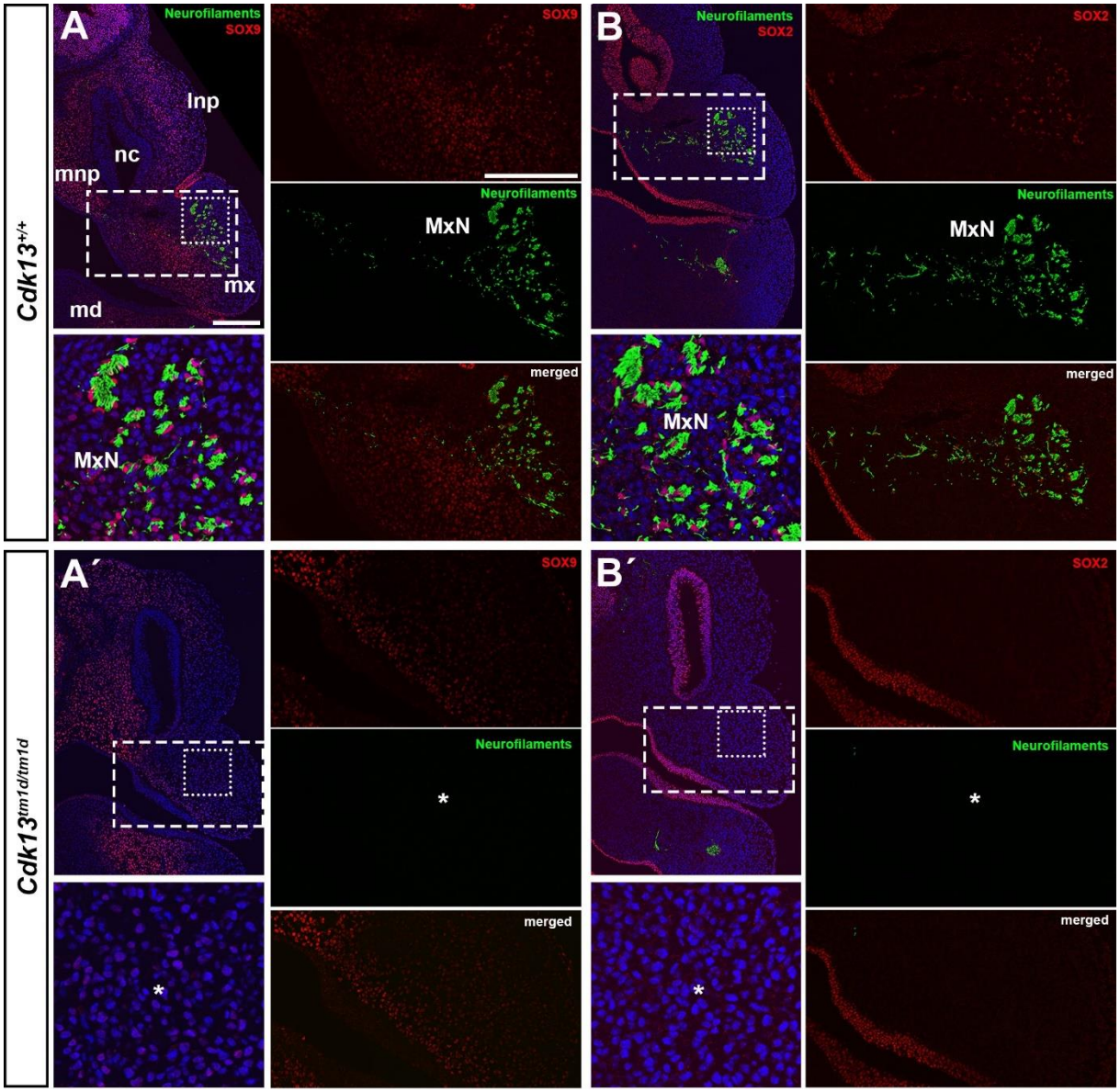

Fig. S8. Immunohistochemical detection of neurofilaments, SOX9 and SOX2 on frontal sections of E11.5 embryos.

(A-B´) Lower power pictures depicting IHC detection of neurofilaments (2H3-antibody) co-stained with SOX9 or SOX2 antibody in the facial prominences at E11.5. White dashed line rectangles highlight individual pictures showing split channels (SOX9 or SOX2 – red; neurofilaments – green) and merged channels (white). White dotted line squares highlight individual higher power pictures with details of maxillary nerves (green) with cells expressing either SOX9 or SOX2 (red). White asterisks focus to the area with missing maxillary branch of the TG nerve. Scale bars: lower power - 200 µm; higher power - 200 µm. lnp– lateral nasal prominence; mnp – medial nasal prominence; md– mandibular prominence; mx– maxillary prominence; MxN – maxillary branch of the trigeminal nerve; nc – nasal cavity.

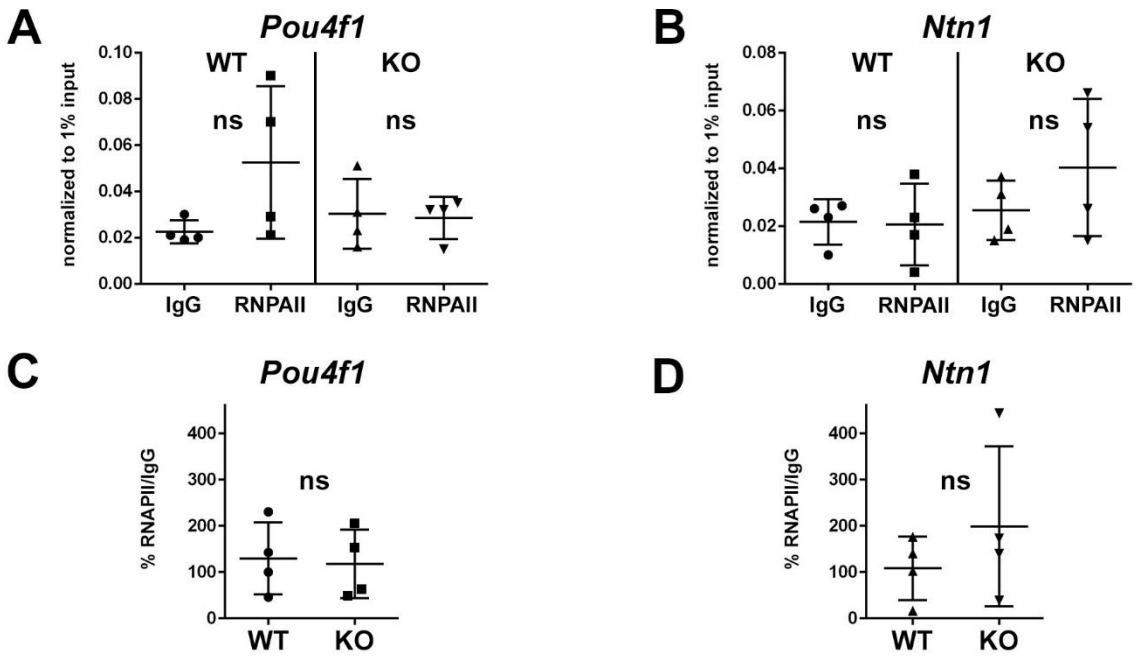

Fig. S9. Depletion of CDK13 leads to lower and higher occupancy of RNAPII within promoters of *Pou4f1* and *Ntn1* genes

(A-B) ChIP analyses for the occupation of RNAPII on the promoters of indicated genes. IgG corresponds to the empty beads control. Experiments are the results of three independent experiments, and qPCR was performed in duplicate. No statistical significance of biological replicates was confirmed at $P < 0.05$. **(C-D)** Percentage of RNAPII binding to promoter sequence was calculated to IgG signal.

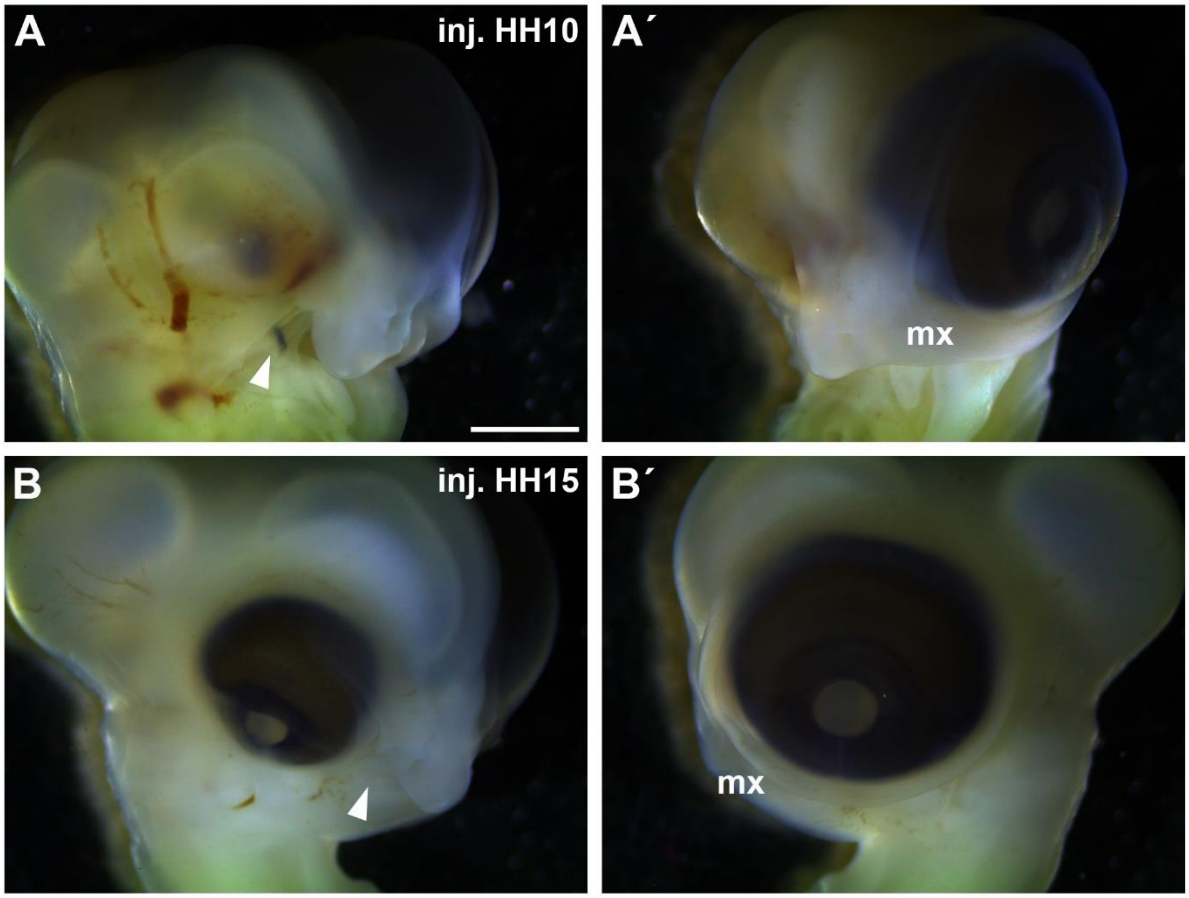

C

injection stage	phenotype frequency
HH10	100 % (6/6)
HH15	86 % (6/7)
HH20	83 % (20/24)

Fig. S10. Chemical inhibition of the CDK12 and CDK13 leads to embryonic facial malformations in chicken model.

(A-B´) Macroscopic pictures focused on lateral regions of the embryonic head. **(A,B)** Missing right maxillary prominences visible in both **(A)** chickens injected at HH10 and **(B)** at HH15 highlighted by white arrowheads. **(A´,B´)** Left control untreated (not injected) sides with no defects. Scale bar: 2 mm. mx – maxillary prominence. **(C)** Table displaying number of chickens with phenotype based on injection stage with THZ531 inhibitor.

Table S1. List of used primary antibodies

Antibody	Retrieval	Dilution	Cat.No.	Company	Notes
2H3	DAKO, pH 9 (IHC)	1:50	AB_2314897	Developmental Studies Hybridoma Bank	Mouse
SOX2	DAKO, pH 9 (IHC)	1:100	2748s	Cell Signaling	Rabbit
SOX9	DAKO, pH 9 (IHC)	1:100	HPA001758	Sigma	Rabbit
Ki67	1% Citrate buffer, pH 6 (IHC)	1:200	RBK027	Zytomed Systems	Rabbit
CDK13	N/A (ICC)	1:100	HPA059241	Sigma	Rabbit
CDK13 N-term	N/A (ICC)	1:100	SAB1302350	Sigma	Rabbit
CDK13	NA (ICC)	1:150	PA5-63692	Invitrogen	Rabbit
F-Actin	N/A (ICC)	1:100	A12379	Thermo Fisher	
2H3	N/A (ICC, Whole Mount IHC)	1:50	AB_2314897	Developmental Studies Hybridoma Bank	Mouse
CDK13	N/A (WB – cell fractionation)	1:3000	HPA059241	Sigma	Rabbit
PARP	N/A (WB – cell fractionation)	1:3000	9542S	Cell Signaling Technology	Rabbit
α-Tubulin	N/A (WB – cell fractionation)	1:10000	7291S	Cell Signaling Technology	Rabbit
Lamin B	N/A (WB – cell fractionation)	1:1000	sc-6217	Santa Cruz Technology	Goat
GAPDH	N/A (WB – cell fractionation)	1:3000	sc-32233	Santa Cruz Technology	Mouse
RNAPII	N/A (ChIP)	1:300	14958S	Cell Signaling Technology	Rabbit

Table S2.

Available for download at
https://journals.biologists.com/dmm/article-lookup/doi/10.1242/dmm.050261#supplementary-data

Table S3.

Available for download at
https://journals.biologists.com/dmm/article-lookup/doi/10.1242/dmm.050261#supplementary-data

Table S4.

Available for download at
https://journals.biologists.com/dmm/article-lookup/doi/10.1242/dmm.050261#supplementary-data